

*Far Ultraviolet Spectroscopic Explorer and Hopkins Ultraviolet Telescope*  
**Observations of Radiative Shocks in the Cygnus Loop<sup>1</sup>**

William P. Blair<sup>2</sup>, Ravi Sankrit<sup>2</sup>, & Sean Tulin<sup>2</sup>

**ABSTRACT**

We report a combination of high and low spectral resolution far ultraviolet spectral data for several groupings of bright radiative shock filaments in the Cygnus Loop supernova remnant. The high resolution spectra were obtained with the *Far Ultraviolet Spectroscopic Explorer (FUSE)* satellite, and cover the 905 – 1187 Å spectral region at 0.1 – 0.3 Å resolution, depending on observing aperture. The low resolution data were obtained with the *Hopkins Ultraviolet Telescope (HUT)* and cover the 850 – 1850 Å spectral region at  $\sim 3$  Å resolution. These data sets complement each other, with the *HUT* data providing the broader context of a wider range of emission lines and the *FUSE* data resolving line profiles from nearby airglow emissions and allowing detailed line profiles to be studied. Relative line intensities and line profiles change on a wide variety of spatial scales. O VI  $\lambda\lambda 1032, 1038$  emission is much more generally distributed than the optical filaments. The *FUSE* data provide direct insight into the effects and variability of self-absorption in the strong resonance lines of O VI and C III  $\lambda 977$ . Variability of the central reversals in O VI with position indicate a patchy O VI distribution, with self-absorption occurring locally within the remnant. Self-absorption in C III could be due to the interstellar medium, the local regions of the remnant, or a combination. We also find evidence for overlying molecular hydrogen absorption effects on some lines, and suggest an interstellar (foreground) origin. It is likely that these effects have had significant impacts on many previous investigations that based their results on the interpretation of low resolution spectral data where these effects could not be seen.

*Subject headings:* ISM: individual (Cygnus Loop) — ISM: nebulae — ISM: supernova remnants — Shock waves

---

<sup>1</sup>Based on observations made with the NASA-CNES-CSA Far Ultraviolet Spectroscopic Explorer. *FUSE* is operated for NASA by the Johns Hopkins University under NASA contract NAS5-32985.

<sup>2</sup>Department of Physics and Astronomy, The Johns Hopkins University, 3400 N. Charles Street, Baltimore, MD 21218

## 1. Introduction

The Cygnus Loop supernova remnant (SNR) provides one of the premiere laboratories for studying astrophysical shock waves and their interaction with the interstellar medium (ISM). Its proximity ( $d = 440_{-100}^{+130}$  pc; see Blair et al. 1999) and large angular size ( $\sim 3.5^\circ$ ) combine to present researchers with a plethora of resolved filamentary structures to study. Also, with little foreground extinction ( $E(B - V) = 0.08$ ; see Fesen, Blair, & Kirshner 1982, Miller 1974), it is one of the few SNRs observable across the entire electromagnetic spectrum, including especially the ultraviolet range that is so often unavailable for galactic SNRs. Finally, its position relatively far off the galactic plane (centered at  $b = -8.6^\circ$ ) eases the problem of possible foreground and background confusion.

Even with extensive study, however, the Cygnus Loop has only revealed its secrets slowly. It is relatively recently, for instance, that we have come to recognize the Cygnus Loop as the remnant of a core collapse supernova, and that the explosion probably occurred in a cavity evacuated by the progenitor star (Charels, Kahn, & McKee 1985, Hester, Raymond, & Blair 1994; Levenson et al. 1997,1998; Bohigas, Sauvageot, & Decourchelle 1999). It is the relatively recent encounter between the SNR blast wave and the cavity wall in its various manifestations (atomic and molecular material distributed in clouds of varying size and density) that is responsible for the dazzling array of structures and phenomena available for study.

Ultraviolet studies of SNRs (and the Cygnus Loop in particular) began in earnest with the advent of the *International Ultraviolet Explorer* satellite (*IUE*) in 1978. Early studies concentrated on bright optical filaments and characterized the phenomenology of the far-UV spectral region, comparing with steady-flow shock models (Raymond 1979; Shull & McKee 1979) to infer shock conditions (Raymond et al. 1980;1981; Benvenuti et al. 1980). Subsequent investigations pushed to fainter filaments (Raymond et al. 1983; Long et al. 1992) and to multi-wavelength investigations of small regions (Raymond et al. 1988; Hester, Raymond, & Blair 1994; Sankrit et al. 2000). Such studies continue on to the present, with the recent work of Danforth, Blair, & Raymond (2001) who have performed a detailed study of the so-called ‘XA’ region in the Cygnus Loop. These studies have shown an increasing appreciation for the complexities involved, including the effects of geometry, shock incompleteness, resonance line scattering, dust grain destruction, and the possibility of nonthermal pressure support.

In this paper, we report further investigations of some of the brightest radiative shock structures in the Cygnus Loop. We seek to better understand the connection between the observed morphology of filaments and their observed spectral characteristics, and what they tell us about the physical conditions and processes in the shocked gas. In this paper, we

present low ( $\sim 3 \text{ \AA}$ ) resolution 900 – 1850  $\text{\AA}$  spectral data from the *Hopkins Ultraviolet Telescope* (*HUT*) and compare with high ( $\sim 0.1 \text{ \AA}$ ) resolution 905 – 1187  $\text{\AA}$  data from the *Far Ultraviolet Spectroscopic Explorer* satellite (*FUSE*). In particular, all of the filaments involved in this study show strong emission lines from O VI  $\lambda\lambda 1031.9138, 1037.6154$ ,<sup>3</sup> which should only be present for shock velocities above  $\sim 160 \text{ km s}^{-1}$ . In general, the results presented here pertain to bright optical filaments that arise from the cooling and recombination zones behind radiative shock waves. *FUSE* observations of a non-radiative shock in the Cygnus Loop are presented by Sankrit & Blair (2002).

Section 2 of this paper describes the relevant observational data and data reductions, while section 3 discusses the *FUSE* data in detail. Section 4 presents a general discussion of these data sets and the conclusions that can be drawn from them. A follow-on paper (Blair et al. 2002) will present a more detailed analysis of the observed line profiles from a subset of the *FUSE* data presented here.

## 2. Observations and Reductions

The *HUT* observations were obtained in 1990 and 1995 and the *FUSE* observations in 2000. Details of the observations are given in Table 1. Below we will describe in separate sections the observations obtained with *HUT* and with *FUSE*.

### 2.1. HUT Spectra

The *HUT* instrument was flown on two space shuttle missions as part of the Astro Observatory payload. The Astro-1 mission (STS-35) occurred in 1990 December and the Astro-2 mission (STS-67) was flown in 1995 March. The characteristics of *HUT* are described by Davidsen et al. (1991) and the details of the instrumental calibration are described by Kruk et al. (1995, 1999). Briefly, *HUT* was a 0.9 m telescope that fed an f/2 beam to a prime focus spectrograph with a microchannel-plate image intensifier and a photon-counting Reticon diode array detector. *HUT* was used to observe the 820 – 1840  $\text{\AA}$  spectral region with a resolution of  $\sim 3 \pm 1 \text{ \AA}$ . It operated from the shuttle as an attached payload, with scientists on the shuttle and at Spacelab Mission Operations Control at NASA/MSFC in Huntsville, Alabama, involved in performing the observations.

---

<sup>3</sup>For convenience, we will sometimes refer to these lines in the text with abbreviated wavelength notation, viz.  $\lambda\lambda 1032, 1038$ .

The optical coatings and spectrograph apertures were different on the two flights. Sensitivity calibrations were obtained from in-orbit observations of white dwarf stars, which were later fitted with theoretical models, scaled from measured optical photometry. The selection of apertures could be used to restrict the region of filaments entering the spectrograph, but no spatial information from within the apertures was available due to the astigmatism intrinsic to the optical system.

During Astro-1, *HUT* was pointed at a bright, radiative shock position on the eastern side of the Cygnus Loop. The reader is directed to the paper by Blair et al. (1991a) for details of this observation. A color image of the Cygnus Loop region of interest is shown in Figure 1, with the position of the *HUT*  $9'.4 \times 116''$  aperture indicated by the red rectangle. As Figure 1 shows, conditions are likely to be spatially variable within the *HUT* Astro-1 aperture, and so three pointings during Astro-2 were dedicated to investigating this potential variability. The three  $12''$  diameter circular aperture positions are also shown in Figure 1. These will be referred to as the *HUT* E1 (MID), E2 (NE), and E3 (SW) positions.

On Astro-2, the Cygnus Loop program was expanded to a number of other positions, including a position on the western side, first observed optically by Miller (1974). This region is shown in Figure 2, and comprises the northern tip of the bright arc of optical filaments known as NGC 6960. While this region contains significant structure along the line of sight from corrugations in the shock front (Hester 1987), it has a fairly simple, smooth morphology in comparison to the chaotic and frothy appearance of the eastern position. A  $10'' \times 60''$  aperture was oriented with its long dimension north-south to select a bright, relatively uniform portion of the filament for study.

The reduction and calibration of these spectra followed standard procedures that have been discussed previously (see Blair et al. 1991a; 1995; Long et al. 1992; Raymond et al. 1995). The Astro-2 *HUT* spectra for the three eastern positions are shown in Figure 3 and the western position is shown in Figure 4. Unfortunately, the Cygnus Loop was only visible during orbital day during Astro-2. Hence, airglow contamination was unavoidable, especially for the larger aperture used on the western filament. At the relatively low spectral resolution of *HUT*, this was a significant problem, especially for lines shortward of  $\text{Ly}\alpha$ . This was one of the motivations for pursuing the higher resolution observations described below.

Line fluxes have been measured primarily using the `splot` task in IRAF<sup>4</sup>, especially in those cases where the lines were free of blending. Selected measurements have also been made with the `specfit` task, developed by G. Kriss (Kriss 1994), which allows careful modeling and fitting of blended line features, based on input assumptions about relative wavelengths and line strengths. This task iterates to minimize  $\chi^2$  using the data error array. This was particularly important in the  $\text{Ly}\beta$ –O VI region, where the lines are blended and where O I

airglow lines are also present in orbital day. This was also important for the O III]  $\lambda 1664$  region, as described below. The derived line fluxes are tabulated in Table 2, where column 2 lists the Astro-1 *HUT* data from Blair et al. (1991a), columns 3–5 are the the Astro-2 eastern Cygnus Loop region data, and column 6 shows the western filament data.

We have scaled the listing in Table 2 relative to the total O III]  $\lambda 1664$  flux having a value of 100 units, for ease of comparison. The advantage of this scaling is that the O III] lines are fairly strong and, being intercombination transitions, are not affected by resonance line scattering. A disadvantage of this, however, is that the *HUT* data obtained in orbital day (note: all of the Astro-2 data) are affected by the O II  $\lambda 834$  airglow line in second order (i.e. at  $1668 \text{ \AA}$ ). We have handled this in the following manner: The O III] lines are formed in a doublet at  $\lambda 1660.8$  and  $\lambda 1666.1$ , and should be observed in the ratio of their statistical weights (0.41:1). It is only the longer wavelength line that gets contaminated by the airglow, and the *HUT* resolution is just sufficient to resolve the  $\lambda 1660.8$  line from the blend. Hence, we have deblended the region with *specfit*, using the observed  $\lambda 1660.8$  line strength and expected ratio to derive the total O III] flux for scaling purposes. The derived absolute fluxes and  $1\sigma$  errors from *specfit* are shown at the bottom of Table 2. We have also handled the blended Si IV–O IV] region in the *HUT* data as described by Blair et al. (1991a).

## 2.2. FUSE Spectra

The *FUSE* satellite was launched 1999 June 24 and began nominal science observations in 1999 December. The characteristics and capabilities of *FUSE* have been described in detail by Moos et al. (2000) and Sahnou et al. (2000a,b). *FUSE* operates over the wavelength range  $905 - 1187 \text{ \AA}$ , with a nominal point source resolution  $R = \lambda/\Delta\lambda = >20,000$  (although somewhat variable with wavelength and spectrograph channel). The velocity resolution for extended sources, however, depends on the spectrograph aperture of choice and assumptions about the filling factor of emission within that aperture (see section 3).

The focal plane of each channel of the *FUSE* instrument contains an aperture plate with three openings into the spectrograph. These include a  $4'' \times 20''$  aperture (dubbed MDRS in *FUSE* nomenclature), a  $1''.25 \times 20''$  aperture (HIRS), and a  $30'' \times 30''$  aperture (LWRS). The apertures are offset in the cross-dispersion direction from one another. Using the middle (HIRS) aperture as reference, the MDRS aperture center is  $100''.5$  in one direction and the

---

<sup>4</sup>IRAF is distributed by the National Optical Astronomy Observatories, which is operated by the Association of Universities for Research in Astronomy, Inc. (AURA) under cooperative agreement with the National Science Foundation.

LWRS aperture center is  $107''8$  in the other direction. For a given coordinate and observation time, the projection of these apertures onto the sky is fixed (within some small tolerance that can be controlled via roll offsets at the time the observations are planned). When expected count rates are below  $2500 \text{ s}^{-1}$ , the detectors are operated in a photon address (time tagged) mode, and separate spectra from all three apertures can be obtained simultaneously. This is the mode used for the observations presented in this paper.

We have used *FUSE* to observe several of the same positions observed with *HUT* during Astro-2, as summarized in Table 1. In each case the MDRS aperture was considered prime and the HIRS and LWRS apertures fell elsewhere within the SNR at positions we consider to be “serendipitous.” In the east, two positions were observed. *FUSE* East Position 1 corresponded in position with the Astro-2 *HUT* middle (E1) position, and the *FUSE* East Position 2 corresponded to the *HUT* NE (E2) position, as shown in Figure 1. The long dimension of MDRS was only approximately aligned with the Astro-1 *HUT* aperture, a compromise made to provide flexibility in scheduling the observations. With the orientation at the time of the observations, we also show the nominal positions of the serendipitous apertures in Figure 1, along with the naming conventions we will use for them.

On the west side, two *FUSE* positions were also observed, but more closely spaced. Figure 2 shows the *FUSE* West Position 1 MDRS aperture near the center of the *HUT* position, with its serendipitous HIRS and LWRS counterparts to the southeast. The long dimension could not be aligned exactly north-south due to *FUSE* spacecraft  $\beta$  (antisun) angle restrictions at the time of the desired alignment. The *FUSE* West Position 2 was exactly one MDRS aperture width ( $4''$ ) due east from the position shown in Figure 2. We have elected not to show this in the Figure to avoid confusion. The intent of this observation was to investigate the effect of relatively small changes in spatial sampling on the derived spectra.

In detail, the situation with the *FUSE* observations is more complicated than described above. *FUSE* consists of four separate optical channels (Moos et al. 2000) and the optical coatings for these channels have been tailored so that two channels are optimized above  $1000 \text{ \AA}$  and two channels are optimized below  $1100 \text{ \AA}$ . There is a generous overlap of all four channels in the  $\sim 1000 - 1100 \text{ \AA}$  range. The long-wavelength channels are referred to as LiF1 and LiF2 while the short wavelength channels are referred to as SiC1 and SiC2.<sup>5</sup> Due to thermal conditions on orbit, the alignment of these four channels is variable, both on an orbital timescale and as the *FUSE* boresight is moved from one region of the sky to another. Large scale changes in alignment with position have been characterized, and are managed

and removed with periodic alignment activities.

The alignment changes that occur on an orbital timescale have also been characterized to a degree, but they are only approximately repeatable and appear to depend on a complicated set of parameters. Since the guide camera on *FUSE* is slaved to the LiF1 channel, it is really the LiF1 apertures that are indicated in Figures 1 and 2. Typical relative alignment changes of the apertures from the other channels relative to LiF1 on the orbital timescale are 3–6", and occur in both the dispersion and cross-dispersion directions. For point sources, observing with the LWRS aperture mitigates these problems in the vast majority of cases since the orbital motions are smaller than the aperture size. However, for apertures placed in extended emission, especially when considering the smaller apertures like MDRS and HIRS, these potential mis-alignments must be taken into account when comparing data from more than one channel.

To minimize these effects, we used the following strategy. Immediately prior to each observation, we aligned the channels by performing a ‘peak-up’ alignment activity on a nearby star (HD 199042). Each multiple orbit observation was then performed without additional alignment, so some small drifting in relative channel alignment would occur. At the end, the satellite was offset back to the nearby star and the channels were re-aligned. This strategy kept the absolute channel alignments accurate to  $\pm 3''$ , with the orbital variations discussed above also present. This means that the emission observed in each channel arises from an adjacent or overlapping spatial region compared with what is seen in LiF1 and varies with time. If spatial variations in the emission are small on the  $\sim 5''$  level, the effect of these misalignments will be small. This may not always be the case in the observed regions of the Cygnus Loop (see below).

Fortunately, the O VI  $\lambda\lambda 1032, 1038$  doublet is strong at the observed positions, and these lines are present in all four channels. We can thus get an indication of potential channel mis-alignments and spatial variations in the emission by comparing the fluxes and line profiles of these lines as observed in the separate channel data. These effects will be discussed at length in section 3.

*FUSE* data are processed with a standardized software pipeline (CalFUSE). The astigmatism of the *FUSE* optical system causes curvature in the cross-dispersion direction. However, for filled apertures, the spectral resolution is already degraded at a level much larger than this effect, so we have ignored any astigmatism or curvature corrections. The standard-

---

<sup>5</sup>Note: LiF and SiC refer to the overcoating materials on the optics for these channels. Furthermore, each detector is sub-divided into two segments, A and B, whose boundaries in wavelength space are offset slightly so that full wavelength coverage is maintained. See section 3 of Moos et al. (2000) for full details.

ized processing works best for typical *FUSE* targets, which are point sources. Because it is difficult for the automated process to assess where the astigmatic spectrum of an emission line source lies on the detectors, the automated processing can sometimes go awry. The data presented here have been reprocessed by us with CalFUSE version 1.8.7, with careful attention paid to the placement of the spectral extraction windows so as to gather all of the relevant emission. We have used the standard flux and wavelength calibrations for the *FUSE* data shown in this paper. We now take a detailed look at the *FUSE* spectra.

### 3. A Detailed Look at the FUSE Data

There are three different apertures for each *FUSE* observation in each of four optical channels. With the significant possibility of small scale spatial variations in velocity or intrinsic line intensities, and with the probability of mis-alignments amongst the channels from thermal effects, we are presented with a complicated situation. Here we choose to provide overview spectra from the LWRS apertures, which have the greatest sensitivity to faint lines and suffer the least from relative channel mis-alignment effects, and then show comparison plots of selected strong lines that permit the degree of spatial variations to be assessed on a case-by-case basis. Throughout this discussion and in the figures, we use the nomenclature in column 1 of Table 1 to address each spectral position, and we use the nomenclature LiF1, LiF2, SiC1, and SiC2 (plus an ‘A’ or ‘B’ designation) to indicate the *FUSE* channel (and detector segment), as appropriate.

#### 3.1. LWRS Overview Spectra

All of the LWRS spectra were serendipitous in the sense that they were not placed on specific filaments. Despite this fact, all four positions contain some optical emission and strong far-UV line detections were obtained. The E1L and E2L LWRS positions correspond to nearly adjacent pieces of sky, the former partially overlapping the (red) western tip of the ‘XA’ region (Danforth et al. 2001) and the latter on a diffuse patch of (blue) optically fainter, possibly higher ionization or less recombined emission to the NE (see Fig. 1). On the western side, positions W1L and W2L lie in a region dominated by red ( $H\alpha$ ) filaments in Figure 2, but for which a complex sight line and other emissions are also present. These two *FUSE* spectra are largely overlapping since the nominal positions of the two 30" aperture positions were only offset by 4". Summary spectra for these positions covering the entire *FUSE* range are shown in Figures 5-8, and measured line intensities are shown in Table 3 (eastern positions) and Table 4 (western positions).

The strong lines in the LWRS spectra, such as O VI  $\lambda\lambda$  1032,1038 and C III  $\lambda$ 977, are broad, with typical full widths at half maximum near  $200 \text{ km s}^{-1}$ . This is broader than the airglow lines ( $\sim 100 \text{ km s}^{-1}$ ), which represent the filled aperture resolution. Hence, the broader lines are intrinsic, due either to Doppler-broadened emission or multiple emitting components within the projected apertures (or a combination). In general, these lines appear non-gaussian, and some show evidence of flat or reversed tops that indicate self-absorption in the ion, quite possibly from other material within the SNR (see below).

The LWRS spectra also show a number of weaker features, seldom if ever seen in SNR spectra previously (cf. Blair et al. 2000; Sankrit et al. 2001). The east side spectra are of somewhat brighter emission and show these lines most clearly, including S VI  $\lambda\lambda$ 933.4,944.5, [Ne VI]  $\lambda\lambda$ 997,999.2,1005.7,1111, S III  $\lambda\lambda$ 1015,1021, S IV  $\lambda\lambda$ 1062.7,1073.0, Si III  $\lambda$ 1115, Si IV  $\lambda\lambda$ 1121,1127 and [Ne V]  $\lambda\lambda$ 1138.5,1146.1. In addition, the C III 1176 Å multiplet of six blended lines is seen in the east side spectra. This is the first report of these lines in the Cygnus Loop, although they were detected in the Vela SNR (Sankrit et al. 2001). The presence of the C III multiplet is somewhat surprising because the lines arise from an excited level and usually require higher densities to be populated. It is a testament to the diffuse source sensitivity of *FUSE*, especially with the LWRS aperture, that these weak lines are detectable.

Finally, we mention the 1085 Å region. The LiF channels have the most sensitivity in this region, but because of small gaps between segments of the *FUSE* detectors, a small wavelength region near 1085 Å is only covered by the SiC channels (see section 3 of Moos et al. 2000). In the Figures, we have pieced in a small portion of data from the SiC1A channel that covers this region. One can see that one or both of N II  $\lambda$ 1084.0 and He II  $\lambda$ 1084.9 are present in the data, but the signal to noise ratio is low.

The overview spectra are useful for obtaining a global perspective of the emissions relative to one another. For instance, the O VI lines should be seen in a ratio of  $I_{1032}:I_{1038} = 2:1$  in optically thin emitting conditions and approach a 1:1 ratio when optically thick conditions occur. The observed ratios at all 4 LWRS positions are intermediate, indicating considerable optical depth in these strong resonance lines. Also, other ions with more than one visible line can provide useful information. S VI is similar to O VI and is expected to be seen at a ratio of  $I_{933}:I_{944} = 2:1$  in optically thin conditions. Although the lines are weak, the ratio does appear to vary and to be between 1 and 2. However, the  $\lambda$ 933 line in particular appears to be narrower than the strong lines, and may indicate overlying  $H_2$  absorption also comes into play. Likewise, as mentioned by Blair et al. (2000) for the SNR N49 in the Large Magellanic Cloud, the 1063 Å line of S IV is expected to be stronger than the 1073 Å line, but is seen to be comparable or weaker. This again points to overlying absorption as being

non-negligible. This issue of overlying absorption will be discussed below, and in Blair et al. (2002), where detailed line profile modeling will be presented.

### 3.2. Strong Line Comparisons

In this section, we concentrate on the strong, well detected O VI doublet and C III lines, comparing their profiles at different positions and in different spectrograph channels to investigate spatial variations in emission line strengths and line profiles. We show three sets of comparison plots, each of which highlights a different aspect of the data. These are: 1) A comparison of the strong O VI  $\lambda 1032$  line between the LiF1A and SiC1A channels. These are shown in Figure 9 (eastern positions) and Figure 10 (western positions), where panels a and b refer to the LWRS profiles, panels c and d show the MDRS profiles, and panels e and f show the HIRS profiles. 2) A comparison of the O VI  $\lambda 1032$  and C III O VI  $\lambda 977$  line profiles both from the SiC1 channel. These are shown in Figure 11 (eastern positions) and Figure 12 (western positions) in a manner similar to Figures 9 and 10. 3) A comparison of the O VI  $\lambda 1032$  and O VI  $\lambda 1038$  line profiles, both from the LiF1A channel. These are shown in Figures 13 and 14. Below we discuss each of these comparisons in detail.

#### 3.2.1. Spatial Variations

The purpose of the first comparison is primarily to assess how similar or different the line profiles are between the two spectrograph channels shown. Such changes could occur for one of several reasons. If the spectrograph channels were misaligned by some amount, the different apertures could sample differing spatial regions of emitting SNR filament. This effect almost certainly occurred for these observations, as discussed in section 2, and might be expected to show up more obviously in the smaller (MDRS or HIRS) aperture data. However, whether actual variations are seen or not depends critically on the spatial structure of each local region being observed and the spatial scale over which significant line profile or intensity variations occur. This could be different for each of the LWRS, MDRS, or HIRS regions sampled in each observation, since each aperture set samples a different location in the filamentary structure. Finally, data from different spectrograph channels may show some variations in detailed line structures due to different fixed-pattern noise, signal-to-noise ratio (since the effective area varies with channel and wavelength), or other detector characteristics. In practice, the last effect can be assessed better by comparing data from all four channels when possible. However, for simplicity, we show two channels here. We choose SiC1 for comparison with LiF1 because SiC1 has higher effective area near O VI and less

severe fixed pattern noise than the SiC2 channel. Also, the SiC channels tend to misalign by a larger amount with respect to the LiF1 channel than does LiF2, so any variations should be more prevalent.

By way of example, refer first to Figure 9a and 9b, which provides this comparison for the *FUSE* E1L and E2L LWRS apertures. Recall these are the two nearly adjacent LWRS positions shown in Figure 1 near the XA region. For E1L, the agreement in O VI $\lambda$ 1032 line intensities and line centroids between LiF1A and SiC1A is good, although some different structure is seen on the red wing in the SiC1A data. In contrast, the E2L comparison shows a roughly 20% change in peak flux and a redward shift of line centroid by  $\sim 30$  km s $^{-1}$  between the two channels. Hence, at this location, the extent of misalignment and/or the degree of spatial variability in emission must have been greater than for E1L. Note that, since the resolution of a filled LWRS aperture is  $\sim 100$  km s $^{-1}$ , these lines are intrinsically broadened.

The eastern MDRS comparison is shown in Figures 9c and 9d. These apertures were located in the midst of very bright radiative emission (see Figure 1) and show very different profiles from those at the LWRS positions discussed above, with flat tops or even central reversals due to self-absorption in the line. The overall profiles at E1M are very similar between the LiF1A and SiC1A channels, although a stronger central reversal is apparent in SiC1A. At E2M, somewhat larger differences are seen between channels, with the redward side of the line stronger in LiF1A and the blueward side stronger in SiC1A. The SiC1A centroid is shifted  $\sim 25$  km s $^{-1}$  redward compared with the LiF1A profile, but the overall line widths are identical. Since the resolution of a filled MDRS aperture is  $\sim 30$  km s $^{-1}$ , the observed line widths again indicate intrinsically broad lines.

Figures 9e and 9f show this comparison for the HIRS aperture positions E1H and E2H in Figure 1, which are not located on any bright optical structures. It is significant that O VI emission is seen at these positions, indicating immediately that O VI emission is distributed quite differently than the optical emission. The signal to noise ratio is lower in these data, but the line profiles are centrally peaked, indicating little or no self-absorption in comparison with the MDRS data (on a bright optical filament). Although systematic differences in line shapes between E1H and E2H appear to be present, the data from the two channels being compared at each position are consistent within the noise, and the line widths are largely intrinsic (since a filled HIRS aperture reproduces the instrumental resolution of  $\sim 15$  km s $^{-1}$ ). Interestingly, there is almost no chance these apertures were co-aligned at a detailed level, since orbital channel alignment drifts of 3-6'' are typical and the aperture is only 1''.25 wide. Hence, the similarity of line shapes between channels indicates relatively small spatial variations at these positions at the several arcsecond scale. This is consistent

with the positions of these apertures on general interfilament regions.

Figure 10 provides the same channel plots as Figure 9, but for the two western data sets. Recall however, that the nominal separation of the two aperture positions is much smaller than for the eastern data sets ( $4''$  perpendicular to the apertures instead of  $\sim 40''$  along the long aperture dimension). The O VI  $\lambda 1032$  fluxes are considerably lower for the western LWRs positions compared with their eastern counterparts. In Figures 10a and 10b, we see generally good consistency in line widths, centroids, and fluxes between the various channels and between the two largely overlapping positions, although some differences in the line peak region of the W1L SiC1A data are apparent. The overall line profiles are less regular in appearance than in the east, indicative of overlying absorption eating away at the blue half of the line profile. It could be a slight change in this absorption with aperture position that contributes to the profile differences between channels seen in Figure 10a.

The western MDRS data are shown in Figures 10c and 10d. In contrast to the profiles on the eastern positions, the western MDRS O VI data appear narrower, single peaked, and somewhat stronger in central line intensity. (The lines are still considerably broader than the filled MDRS resolution of  $30 \text{ km s}^{-1}$ , however.) These differences could be intrinsic, but we note the presence of a faint blueward bump in all of the profiles. This could be understood if the overall line widths were comparable in the west, but the self-absorption was offset to negative velocities, affecting the blue wing of the line profile instead of causing a flat topped or centrally-reversed O VI line profile. In this scenario, the stronger line peak would correspond to the red half of the line experiencing less self-absorption and thus appearing stronger.

It appears the channel alignment was substantially off for the W1M pointing. This can be seen from the following comparison. The solid lines in Figures 10c and 10d are the LiF1A MDRS profiles from two positions on the bright western filament. Since the LiF1 channel is used for guiding, we have high confidence that these two profiles represent emission from adjacent  $4''$  pieces of sky, and the line profiles are indeed very similar in intensity and line shape. Hence, the large difference between channels indicated in Figure 10c must be due to channel misalignments between LiF1 and SiC1, with SiC1 having been on a region of fainter O VI emission. (Recall that a more significant difference was also seen for the corresponding LWRs comparison above—see Figure 10a.) A much smaller variation between channels is seen for the W2M position, indicating much closer co-alignment of channels for this observation.

The HIRS aperture observations, shown in Figures 10e and 10f, are of low signal to noise, but show a systematic and interesting effect. The line profiles appear as broad or broader than the MDRS profiles, and possibly the same breadth as the LWRs profiles, despite the smaller filled-aperture resolution of HIRS. Also, whatever the channel mis-alignments were,

they were such that the SiC1 HIRS apertures were on brighter O VI emission compared to the LiF1 apertures shown in Figure 2.

### 3.2.2. Comparison of O VI and C III Line Profiles

One of the key comparisons from the *FUSE* data involves the O VI lines, whose emissivity peaks near 300,000 K, and the C III  $\lambda 977$  line, which arises in gas near 50,000 K. We concentrate on O VI  $\lambda 1032$ , which lies in a region relatively free from possible overlying  $H_2$  absorption. (The 1032 Å and 1038 Å lines will be compared in the next section.) Since the C III region is only sampled by the SiC channels, we choose the SiC1 channel for this comparison because it has less fixed pattern noise than SiC2. Using the observed O VI  $\lambda 1032$  and C III  $\lambda 977$  from the same channel ensures that we are sampling the same spatial region for both comparison lines, although the region being sampled may be offset slightly from the positions indicated in Figures 1 and 2 because of channel drift. In Figures 11a-f and 12a-f, we show these comparisons for the various apertures and for the eastern and western filaments.

In Figure 11a and 11b, we see very different behavior in these two lines for the LWRS aperture positions E1L and E2L, even though the apertures are nearly adjacent on the sky. The overall ratio of C III:O VI  $\lambda 1032$  changes by a factor of  $\sim 2$  between the positions. At the E1L position, the line centroids in velocity space and line widths are nearly the same, while for E2L, C III is narrower and its centroid is red-shifted by  $\sim 30 \text{ km s}^{-1}$ . Given the large area of the apertures and their relatively close spacing on the sky, this is quite a dramatic change. Based on the optical data, which shows the E1L aperture overlapping the (red)  $H\alpha$  portion of the XA position, one might have expected the C III emission to be stronger here instead of at E2L. A possible explanation of this dichotomy is that resonance line scattering is more severe on the brighter optical filament, which decreases the relative amount of C III at this position, as discussed by Danforth et al. (2001).

Figures 11c and 11d show the MDRS apertures for comparison. The signal to noise ratio is lower but the resolution is higher. All of the observed profiles are non-gaussian, with the O VI lines at both positions and the C III line at E2M clearly showing central reversals indication of self-absorption by each ion near zero velocity. (A flattening of the peak of the profile or possible central reversal for C III at the E1M position is not precluded by the rather noisy data.) The line centroids are close at both positions, and no dramatic differences in line widths are evident, although C III may be somewhat narrower at E1M.

We show the eastern HIRS aperture comparison in Figures 11e and 11f. The signal to

noise ratio is low, but O VI is definitely detected at both positions. C III appears stronger for E1H and is not reliably detected at E2H, commensurate with appearances in Figure 1 where faint blue emission is seen in the E1H region.

The comparison of O VI and C III for the western positions is shown in Figure 12. The C III line is comparable to or stronger than O VI  $\lambda 1032$  in the western LWRS data (see Figures 12a,12b), somewhat in contrast to the east side LWRS positions. A central absorption is seen centered at about  $+40 \text{ km s}^{-1}$  in the C III lines at both LWRS positions that is not clearly duplicated in the O VI profiles.

Interestingly, the MDRS data on the bright western filament (Figures 12c and 12d) are very different from the eastern data, and the C III and O VI profiles at each positions are very different from each other. For instance, at W1M, the O VI line is narrow and weak, and centrally peaked (although perhaps with a broad base) while the C III line is strong and broad with a central reversal! Recall from Figure 10c that the alignment if SiC1 with LiF1 was likely not very good, so this comparison may be a region somewhat off of the bright filaments, but it is quite unlike the eastern bright filament observations. For the W2M position (Figure 12d), the SiC channel must have been positioned more on the bright filament, as the O VI intensity is comparable to C III, but the other characteristics of the W1M data persist, with O VI narrower and centrally-peaked while C III is broader with a central reversal. The central dips in C III are red-shifted by  $\sim 25 \text{ km s}^{-1}$ , consistent with but not as high as those seen in the LWRS C III lines above. This may be a characteristic of the overlying absorber on the west side.

Finally, the western HIRS data are shown in Figures 12e and 12f. Again they are low signal to noise, due to the smaller aperture area and because the serendipitous positions placed them in a faint region. However, C III and O VI are detected at both locations, and the profiles appear to be as broad as those seen in the LWRS data. This probably indicates that material at a range of projected velocities to the sightline are being sampled at this position considerably behind the main body of filaments. There is a slight indication that C III shows a central reversal while O VI does not, similar to the other positions on the west side.

### 3.2.3. Comparison of O VI Line Profiles

The third comparison we make is between the two O VI lines,  $\lambda 1032$  and  $\lambda 1038$ . Both lines are transitions from the ground state of  $\text{O}^{5+}$  and are expected to have the same line shape. However, the ratio of their intensities will depend of the line optical depth. In

optically thin conditions, the line ratio  $F_{1032}:F_{1038}$  is equal to two, the ratio of the oscillator strengths. For higher optical depths, the ratio approaches a value of one. Thus, in principle, the observed line ratio can be used to estimate the line optical depth. In practice we find the situation is more complicated.

The O VI line comparison plots are shown in Figures 13-14, for the eastern and western positions, respectively. Both lines are taken from the LiF1 channel data. There is a definite tendency for the  $\lambda 1038$  line to be narrower than the  $\lambda 1032$  line either slightly or significantly (from one position to another) or to otherwise show different structure from its short wavelength counterpart. This points clearly to the presence of overlying absorption affecting the observed  $\lambda 1038$  lines.

Many *FUSE* observations of continuum sources have demonstrated clearly that the  $\lambda 1038$  region of the spectrum can be severely impacted by molecular hydrogen,  $H_2$  (Oegerle et al. 2000; Richter et al. 2001). Specifically,  $H_2$  has Lyman band  $J=1$  transitions from the lowest vibrational state at rest wavelengths of  $1037.15 \text{ \AA}$  (5-0 R(1)) and  $1038.16 \text{ \AA}$  (5-0 P(1)), which can impact the O VI  $\lambda 1037.62$  line. Thus, we attribute the narrower  $\lambda 1038$  profiles to  $H_2$  absorption, with small differences between positions arising from small relative Doppler shifts of emitting and absorbing components. Interestingly, however, despite the systematic absorption of  $\lambda 1038$  relative to  $\lambda 1032$ , which would tend to increase the  $F_{1032}:F_{1038}$  ratio there is a clear tendency for the observed ratio to appear  $<2$ , especially for the western positions. This indicates substantial and variable optical depth in the cores of these lines.

The eastern positions provide some useful insights into this observed effect. The LWRS data in Figures 13a and 13b show broad, regular profiles, with widths of  $\lambda 1038$  slightly if at all narrower than  $\lambda 1032$ . This indicates relatively little impact from overlying  $H_2$  absorption, and the observed relative line intensities are somewhat less than 2, but not dramatically so. Hence, at the fairly diffuse positions sampled by these large apertures, the mean optical depth is not high.

The eastern MDRS positions are on the optically brightest filaments and show quite a different character. The  $\lambda 1038$  lines are narrower, and at the E2M position in particular the line shape is very different than for  $\lambda 1032$ , indicating significant overlying absorption. Significant central dips are seen, especially in  $\lambda 1032$ , and the flux ratio of  $\lambda 1032$  to  $\lambda 1038$  is much closer to 1, implying higher optical depth. In contrast, the eastern HIRS positions (Figures 13e and 13f) have roughly gaussian profiles and are close to a 2:1 ratio, consistent with the position of these apertures in sightlines of lower density and less overlying absorption. The central reversals at the MDRS positions indicates significant optical depth in O VI along these sightlines, while the narrower width of  $\lambda 1038$  indicates bracketing  $H_2$  absorption by the  $J=1$  transitions mentioned above.

The behavior of this line ratio with position in conjunction with the shapes of the observed profiles provides an important clue to what is occurring at the observed positions. The presence of self-absorption in O VI is correlated with ratios of  $F_{\lambda 1032}:F_{\lambda 1038} < 2$ . The same atomic physics that causes O VI to be observed in a 2:1 ratio when viewed in emission from optically thin gas also causes it to absorb in a 2:1 ratio. That is,  $\lambda 1032$  is more affected by self-absorption by overlying O VI than is  $\lambda 1038$ , which drives the observed ratio below 2. Thus, the intrinsic (emitted) O VI line ratios may be much closer to the optically thin ratio than what is observed. The fact that this effect appears to be more prevalent toward the brightest optical filaments than for the apertures in more diffuse emission implicates overlying gas in close proximity to the bright optical filaments as the primary self-absorber.

The west side positions are shown in Figure 14. The LWRS O VI profiles (Figures 14a and 14b) track each other very well and are observed in a nearly 1:1 ratio. This indicates significant optical depth at both LWRS positions and across a fairly broad velocity range. From the overall line profiles, there is some indication of either multiple broad components blending together or of a blue-shifted, partial central reversal from self-absorption. In this case, since LWRS data seem less prone to showing self-absorption (because of lower filled aperture resolution and a greater admixture of material being sampled), and because the  $\lambda 1032$  and  $\lambda 1038$  lines behave in a similar manner, it would appear that the multiple components model may be the correct interpretation for this position. The position of these apertures somewhat behind the primary shock front is also consistent with this interpretation.

The MDRS apertures (Figures 14c and 14d) sample the bright, edge-on optical filament region. The  $\lambda 1032$  and  $\lambda 1038$  lines are close in peak intensity, again indicating high optical depth, although the  $\lambda 1038$  lines are marginally narrower than  $\lambda 1032$  implying some affect from overlying  $H_2$  absorption. Also, as discussed earlier, a faint blue bump on the wing of  $\lambda 1032$  either indicates a weak second component along this line of sight or possibly a broader intrinsic line that has been heavily impacted by self-absorption. The absence of this component on the blue wing of  $\lambda 1038$  is likely due to an  $H_2$  absorption expected near this velocity, as indicated by Sankrit & Blair (2002) for filaments in the northeastern Cygnus Loop.

One last surprise is indicated by the western HIRS positions, as seen in Figures 14e and 14f. Again, as with other HIRS data, the signal to noise ratio is not high. However, the lines appear to be fairly broad, with the W1H lines appearing consistent with a 2:1 ratio and W2H being weaker and consistent with a ratio of 1:1. While higher precision measurements would be needed to confirm this, it serves to demonstrate the variability and potential unpredictability of observations based on the optical appearances of the sampled material.

#### 4. Discussion

In this section, we discuss some of the general conclusions that can be derived from these spectra. One point that is immediately obvious from inspection of these data is that O VI emission in the Cygnus Loop is distributed in a very different manner than the bright optical filaments. This has been known on large spatial scales (and at poor spatial resolution) even from Voyager Ultraviolet Spectrometer data (Blair et al. 1991b; Vancura et al. 1993), but it continues to be true on the smaller sampling scales of the *FUSE* serendipitous aperture positions. This can be seen in Table 5, where O VI and C III surface brightness numbers scaled per square arcsecond are given for the different positions. As one specific example, the O VI surface brightness for the eastern HIRS apertures (in regions of very faint optical emission) are only lower than those of the eastern MDRS apertures (which were situated on bright optical emission) by a factor of  $\leq 2$ . This points to the widespread presence of shocks in excess of  $160 \text{ km s}^{-1}$ , only some of which have recombined to the point of producing bright optical line emission. It may also point to the presence of considerable non-radiative shock emission, for which bright O VI and other UV line emission is seen even though their optical output is limited to faint Balmer line emission (Long et al. 1992; Hester et al. 1994; Sankrit et al. 2000). Indeed, the relatively faint, red filament arcing northward from aperture E2L in Figure 1 is likely a non-radiative shock from elsewhere along the line of sight seen in projection.

The optical appearance of SNR filamentary structures continues to be one of the primary selection criteria for new observations. However, work such as the [Ne V]  $\lambda 3425$  imaging by Szentgyorgyi et al. (2000) and the results presented here demonstrate clearly a partial decoupling between the bright regions of optical emission and the bright UV emission. This partial decoupling causes significant uncertainty in interpretation (see also Danforth et al. 2001). One can only hope that, when observing a bright optical (radiative) filament, its emission dominates the emission from the observed sightline and provides a representative measurement. However, this assumption is not always valid. (See, for instance, the C III emission profile through the middle of the Vela SNR presented by Sankrit et al. 2001.)

We next discuss spatial variations in line emission. The three Astro-2 *HUT* observations in the eastern region (Figure 3) were designed to study variations within the large Astro-1 *HUT* aperture. These three positions correspond to different sub-structures within the bright filament. Table 2 shows the comparison, and the changes between the three apertures are significant. Differences of 25–50% in the relative intensities of many of the strong lines between apertures are not uncommon, although some of these comparisons are compromised by nearby airglow emissions that affect the accuracy of the individual measurements. The question remains as to what these variations mean since the trends are not always consistent.

The variations in O VI intensity with position, for instance, do not correlate well with the variations seen in N V. Apparently we are seeing a combination of intrinsic spatial variations and other factors that confuse the picture.

Comparing the eastern and western *HUT* observations is also interesting (Figure 4 and Table 2). While there are differences in some of the strong line intensities, the overriding reaction is one of general similarity, especially when concentrating on some of the fainter, intercombination lines that are not affected by resonance line scattering. Even from the low resolution data, one begins to derive a picture where overlying variations in resonance line scattering may be affecting the relative line intensities of many strong lines. This was one of the primary conclusions of Danforth et al.’s (2001) detailed study of the XA region in the Cygnus Loop as well.

The *FUSE* data provide a new tool for investigating shocks. The combination of high spectral resolution and access to the far-UV lines (especially O VI and C III) is not a capability that has been available previously. Even with the *HUT* data described above, the significant contamination by nearby airglow lines caused a significant problem in determining accurate total O VI measurements, let alone an accurate O VI line ratio to assess optical depth. The *FUSE* data not only permit separation of key lines from airglow contamination, but allow the detailed line profiles to be measured and compared. The *FUSE* data have a number of important ramifications.

The *FUSE* data sample spatial variations on a range of scales, from the separate specific aperture locations selected to the serendipitous aperture spacing of a few arcminutes to the scale of 3–6" sampled by the thermal channel alignment variations. From Figures 9 and 10, we conclude that the variations on the smallest spatial scales sampled are generally small. The most significant exception is at W1M (Figure 10c), where a substantial difference in O VI intensity is seen between LiF1A and SiC1A. In this particular case, it appears likely that the SiC channels were misaligned toward the west so that the SiC channels were just on the leading edge of the western shock front. The conclusion is supported by the W2M observation, taken directly after W1M: when the LiF1 aperture was moved 4" east, the SiC channel was moved onto the bright filament and the O VI intensities are comparable (Figure 10d). This indicates that the largest spatial variations in relative line intensities correlate with stepping across an optical feature. However, once one is sampling different portions of the post-shock flow, the spatial variations are relatively small, at least at the spatial scales sampled by the *FUSE* apertures.

An important aspect of the story told by the *FUSE* data is that a significant fraction of the observed line intensity variations seen in lower resolution data can be attributed to variations in overlying absorption (either self-absorption in a resonance line or overlying H<sub>2</sub>

absorption) rather than intrinsic variations. This is particularly apparent in the MDRS aperture comparisons, which were all on bright filaments. The C III line profiles all have *significant* central reversals at essentially zero velocity, due to C III self-absorption. Hints that this is also true for the LWRS and HIRS data are present, although the comparison is hampered by lower resolution (LWRS) and lower signal to noise ratio (HIRS). Since C III is a strong interstellar absorption line, it is probable that a significant portion if not all of this self-absorption is due to intervening ISM. (We note, however, that the dramatic change in relative C III intensity between E1L and E2L, Figures 11a and 11b, cannot be due to realistically to ISM variations on such a small spatial scale.)

O VI on the other hand shows more variation in profile. The eastern MDRS data show significant central reversals in O VI (Figures 11c,d), while the western MDRS data do not (Figures 12c,d). This indicates that O VI self-absorption is patchy, and is probably associated with overlying absorption from within the Cygnus Loop itself as opposed to an ISM interpretation. The most significant O VI self-absorption occurs for the E1M and E2M positions on the bright eastern filament, perhaps indicating the self-absorption occurs locally in overlying gas associated directly with this region. The higher  $F_{1032}:F_{1038}$  ratios for the eastern HIRS and LWRS data in comparison with the MDRS data support this conclusion.

Another potential complication for lines below 1108 Å is the possibility that molecular hydrogen absorption is affecting the observed line intensities and/or profiles. In a future paper, we will investigate detailed modeling of the *FUSE* line profiles to understand these effects. For now we mention the following qualitative points. H<sub>2</sub> absorption is normally assessed with a background continuum source, providing access to a wide range of Lyman and Werner band transitions for confirming and characterizing the H<sub>2</sub> (cf. Sembach 1999). With only a handful of emission lines to use as a ‘background source,’ it is more difficult to assess this effect and (for instance) determine a unique model of the absorbing H<sub>2</sub>. In certain situations, such as with circumstellar disks (Roberge et al. 2001; Lecavelier des Etangs et al. 2001), the observed O VI emission lines are broad enough that discrete H<sub>2</sub> absorption lines can be seen and characterized. In the observations reported here, however, the situation is somewhat different: there is a systematic tendency for O VI  $\lambda 1037.6$  to be narrower and/or have significantly different line profile structure than O VI  $\lambda 1032$ . This is because the O VI emission is only broad enough that the two H<sub>2</sub> J=1 lines bracketing the O VI  $\lambda 1037.6$  rest wavelength absorb the wings of the profile.

The region near N III  $\lambda 991.5$  can be impacted by H<sub>2</sub> absorption as well, especially on the blue side where a J=0 H<sub>2</sub> transition occurs. The C III  $\lambda 977.0$  line, on the other hand, sits in a ‘window’ in the H<sub>2</sub> absorption pattern (although it is strongly affected by self-absorption). There is evidence from the overview spectra (Figures 5–8) that N III is narrower than C III

and weaker than expected with respect to C III from standard metallicity shock models such as those of Hartigan, Raymond, & Hartmann (1987). If these effects occurred only in the western data, it would be tempting to suggest that the molecular cloud present on this side of the Cygnus Loop (DeNoyer 1975) is the source of this material. However, the effect appears to be prevalent in the eastern data as well, pointing toward a foreground ISM component of H<sub>2</sub> absorption across the face of the Cygnus Loop that has not been recognized previously.

The seriousness of resonance line self-absorption and possible impacts of H<sub>2</sub> absorption below 1108 Å, as demonstrated by a comparison of the *HUT* and *FUSE* data, has some immediate ramifications. The relative intensities of various far-UV emission lines have been important diagnostics of everything from shock velocities to abundances to dust grain destruction to thermal versus nonthermal pressure support in the post-shock gas. At low resolution, one measures only the relative (attenuated) line intensities. With *FUSE* data, one can assess the effects of this attenuation and correct the observed line ratios to obtain a closer approximation of the intrinsic emission. As a specific example, the observed O VI:C III ratio at *FUSE* position E1M (Table 5) is 3.95. By using the observed line widths and assuming Gaussian line profiles to assess the ‘missing’ flux in each line, we estimate a 60% attenuation of C III λ977 and a 25% attenuation of the total O VI flux. Hence, the intrinsic ratio is closer to 3.09, indicating a larger admixture of slower shocks within the observed position than would have been estimated without the correction.

To summarize, the observations presented here have numerous important ramifications. We have shown clearly that the distribution of O VI emission is much different from the bright optical emission on small and intermediate spatial scales. This points to widespread shocks at velocities in excess of 160 km s<sup>-1</sup> only some of which have become bright optically. We have also demonstrated the variability of relative emission line intensities on many spatial scales. However, these changes are not necessarily due to intrinsic changes, but can also be due to variations in overlying absorption with position. In some cases this absorption may occur locally within overlying gas in the Cygnus Loop although contributions from ISM absorptions are likely in the cooler ions and H<sub>2</sub>. Observations such as those from *FUSE* presented here provide the ability to assess overlying absorption and permit more accurate estimates of the intrinsic relative line intensities. This in turn will lead to improved assessments of the physical conditions and processes involved in the interactions of the Cygnus Loop blast wave with its surroundings.

It is a pleasure to thank the *FUSE* operations team at JHU for their efforts in obtaining these data, and to once again thank the astronauts and support personnel for the Astro-1 and Astro-2 missions. The *HUT* project was funded by NASA contract 5-27000, and the *FUSE* project is funded for U.S. investigators by NASA contract NAS5-32985, both to the

Johns Hopkins University.

## REFERENCES

- Benvenuti, P., Dopita, M. A., & D’Odorico, S. 1980, *ApJ*, 238, 601
- Blair, W. P., et al. 2000, *ApJ*, 538, L61
- Blair, W. P., et al. 1991a, *ApJ*, 379, L33
- Blair, W. P., Long, K. S., Vancura, O., & Holberg, J. B. 1991b, *ApJ*, 374, 202
- Blair, W. P., Raymond, J. C., Long, K. S., & Kriss, G. A. 1995, *ApJ*, 454, L35
- Blair, W. P., Sankrit, R., Raymond, J. C., & Long, K. S. 1999, *ApJ*, 118, 942
- Blair, W. P., et al. 2002, in preparation
- Bohigas, J., Sauvageot, J. L., & Decourchelle, A. 1999, *ApJ*, 518, 324
- Chales, P. A., Kahn, S. M., & McKee, C. F. 1985, *ApJ*, 295, 456
- Danforth, C. W., Blair, W. P., & Raymond, J. C. 2001, *AJ*, 122, 938
- Danforth, C. W., Cornett, R. H., Levenson, N. A., Blair, W. P., & Stecher, T. P. 2000, *AJ*, 119, 2319
- Davidson, A. F., et al. 1992, *ApJ*, 392, 264
- DeNoyer, L. K. 1975, *ApJ*, 196, 479
- Fesen, R. A., Blair, W. P., & Kirshner, R. P. 1982, *ApJ*, 262, 171
- Hartigan, P., Raymond, J., & Hartmann, L. 1987, *ApJ*, 316, 323
- Hester, J. J. 1987, *ApJ*, 314, 187
- Hester, J. J., Raymond, J. C., & Blair, W. P. 1994, *ApJ*, 420, 721 (HRB)
- Kriss, G. A. 1994, in *Astronomical Data Analysis Software and Systems III*, ASP Conf. Series, 61, 437
- Kruk, J. W., Durrance, S. T., Davidson, A. F., Blair, W. P., Espey, B. R., & Finley, D. S. 1995, *ApJ*, 454, L1
- Kruk, J. W., Brown, T. B., Davidson, A. F., Espey, B. R., Finley, D. S., & Kriss, G. A. 1999, *ApJS*, 122, 299
- Lecavelier des Etangs, A., et al. 2001, *Nature*, 412, 706
- Levenson, N. A., et al. 1997, *ApJ*, 484, 304

- Levenson, N. A., Graham, J. R., Keller, L. D., & Richter, M. J. 1998, *ApJS*, 118, 541
- Long, K. S., et al. 1992, *ApJ*, 400, 214
- Miller, J. S. 1974, *ApJ*, 189, 239
- Moos, H. W., et al. 2000, *ApJ*, 538, L1
- Oegerle, W. R., et al. 2000, *ApJ*, 538, L23
- Raymond, J. C. 1979, *ApJS*, 39, 1
- Raymond, J. C., Black, J. H., Dupree, A. K., Hartmann, L. H., & Wolff, R. S. 1980, *ApJ*, 238, 881
- Raymond, J. C., Black, J. H., Dupree, A. K., Hartmann, L. H., & Wolff, R. S. 1981, *ApJ*, 246, 100
- Raymond, J. C., Blair, W. P., Fesen, R. A., & Gull, T. R. 1983, *ApJ*, 275, 636
- Raymond, J. C., Blair, W. P., & Long, K. S. 1995, *ApJ*, 454, L31
- Raymond, J. C., Hester, J. J., Cox, D. P., Blair, W. P., Fesen, R. A., & Gull, T. R. 1988, *ApJ*, 324, 869
- Richter, P., Savage, B. D., Wakker, B. P., Sembach, K. R., & Kalberla, P. M. W. 2001, *ApJ*, 549, 281
- Roberge, A., et al. 2001, *ApJ*, 551, L97
- Sahnow, D., et al. 2000a, *ApJ*, 538, L7
- Sahnow, D., et al. 2000b, *Proc. SPIE*, 4013, 334
- Sankrit, R., & Blair, W. P. 2002, *ApJ*, in press
- Sankrit, R., Blair, W. P., Raymond, J. C., & Long, K. S. 2000, *AJ*, 120, 1925
- Sankrit, R., Shelton, R. L., Blair, W. P., Sembach, K. R., & Jenkins, E. B. 2001, *ApJ*, 549, 416
- Sembach, K. R. 1999, in the *Stromlo Workshop on High Velocity Clouds*, ASP Conf. Series 166, eds. B. K. Gibson & M. E. Putman (San Francisco: ASP), p. 243
- Shull, J. M., & McKee, C. F. 1979, *ApJ*, 227, 131
- Szentgyorgyi, A., Raymond, J. C., Hester, J. J., & Curiel, S. 2000, *ApJ*, 529, 279
- Vancura, O., Blair, W.P., Raymond, J.C., & Holberg, J.B. 1993, *ApJ*, 417, 663

## Figure Captions

**Fig. 1:** A three-color image of the eastern portion of the Cygnus Loop of interest to this paper. For this image, ground-based  $H\alpha$  (red) and [O III]  $\lambda 5007$  (green) images have been combined with a far-ultraviolet image from the Ultraviolet Imaging Telescope (blue). The UV image is dominated primarily by C IV  $\lambda 1550$ . See Danforth et al. (2000, 2001) for details. The red rectangle shows the position of the *HUT* (Astro-1) aperture, while the three red circles show the *HUT* Astro-2 positions (label E1, E2 and E3). The black rectangles show the primary (MDRS) *FUSE* East aperture positions E1M and E2M whose centers correspond with the *HUT* E1 and E2 positions. The yellow apertures show the serendipitous *FUSE* HIRS (E1H) and LWRS (E1L) aperture locations for E1M, and the green apertures are the same for *FUSE* E2M. North is up, and East is to the left, and a scale bar is shown.

**Fig. 2:** A three-color image of the northern end of the western Cygnus Loop region. The color-filter combinations are the same as Figure 1, although the color balance is somewhat different. The red rectangle represents the *HUT* (Astro-2) aperture location, while the black rectangle shows the *FUSE* W1M (MDRS) aperture. The yellow apertures show the serendipitous *FUSE* HIRS (W1H) and LWRS (W1L) aperture locations. The *FUSE* W2M, W2H and W2L apertures (not shown) are the same aperture pattern as shown for W1, but positioned one MDRS aperture width ( $4''$ ) due east (left) to search for fine scale structure in the line profiles. North is up, and East is to the left, and a scale bar is shown. (These optical data are courtesy of N. Levenson.)

**Fig. 3:** Astro-2 *HUT* spectra for three positions from within the Astro-1 aperture position, as indicated in Figure 1. The top panel is the NE position, the middle panel shows the middle position, and the bottom panel shows the SW position. Some of the stronger SNR lines are indicated on the middle panel. The strong lines that go off-scale are due to airglow emissions. Some of the weaker features are intrinsic and some are airglow. Refer to Table 2 for details, or to Figure 4, where more detailed labeling is provided. The MID position corresponds to *FUSE* E1M MDRS aperture, and NE corresponds to *FUSE* E2M.

**Fig. 4:** Astro-2 *HUT* spectrum of the Cygnus Loop western filament indicated in Figure 2.

**Fig. 5:** Astro-2 *FUSE* LWRS overview spectrum of the Cygnus Loop eastern region E1L. The data are displayed after binning over 8 pixels. The top panel shows the SiC1B channel data. The middle panel shows primarily LiF1A data, although a small section of SiC1A data are used in the 1080 - 1092 Å region. The bottom panel shows data from the LiF2A channel. In the middle panel, we also show the weak line regions offset upward by 5 units, and scaled up by a factor of 10 relative to the O VI lines. Earth symbols designates

residual airglow lines in the spectrum.

**Fig. 6:** Same as Figure 5, but for the E2L position. Note that the C III line in the top panel goes off-scale, but its peak flux is indicated.

**Fig. 7:** Same as Figure 5, but for the W1L position. Note that the C III line in the top panel goes off-scale, but its peak flux is indicated. Also, the faint line regions in the middle panel have been offset by 3 units and scaled up by a factor of 4.

**Fig. 8:** Same as Figure 5, but for the W2L position. As in Figure 7, the faint line regions in the middle panel have been offset by 3 units and scaled up by a factor of 4.

**Fig. 9:** *FUSE* channel comparison plots for O VI  $\lambda$  1032, as viewed by the LiF1A channel (solid lines) and SiC1A channel (dashed lines). Panels a and b show LWRS data from E1L and E2L, panels c and d show MDRS data from E1M and E2M, and panels e and f show profiles from the HIRS E1H and E2H positions (see Figure 1). These plots can be used to assess channel mis-alignments and possible spatial variations in line intensities.

**Fig. 10:** Analogous to Figure 9, but for the west side data. See Figure 2 for aperture locations.

**Fig. 11:** *FUSE* line comparison plots for O VI  $\lambda$  1032 (solid lines) and C III  $\lambda$  977 (dashed lines), as viewed by the SiC1 channel. Panels a and b show LWRS data from E1L and E2L, panels c and d show MDRS data from E1M and E2M, and panels e and f show profiles from the HIRS E1H and E2H positions (see Figure 1). These plots can be used to assess the relative line centroids, fluxes, and profiles of C III and O VI since the data correspond to a single set of aperture positions on the sky.

**Fig. 12:** Analogous to Figure 11, but for the west side data. See Figure 2 for approximate aperture locations.

**Fig. 13:** *FUSE* line comparison plots for O VI  $\lambda$  1032 (solid lines) and O VI  $\lambda$  1038 (dashed lines), as viewed in the LiF1A channel. Panels a and b show LWRS data from E1L and E2L, panels c and d show MDRS data from E1M and E2M, and panels e and f show profiles from the HIRS E1H and E2H positions (see Figure 1). Since both lines are from the same ion and same spectrograph channel, variations in line shapes must be due to variations in overlying absorption, primarily from  $H_2$ .

**Fig. 14:** Analogous to Figure 13, but for the west side data. See Figure 2 for aperture locations.

Fig. 1.— Figure 1: Large color EPS file kept separately from text.

Fig. 2.— Figure 2: Large color EPS file kept separately from text.

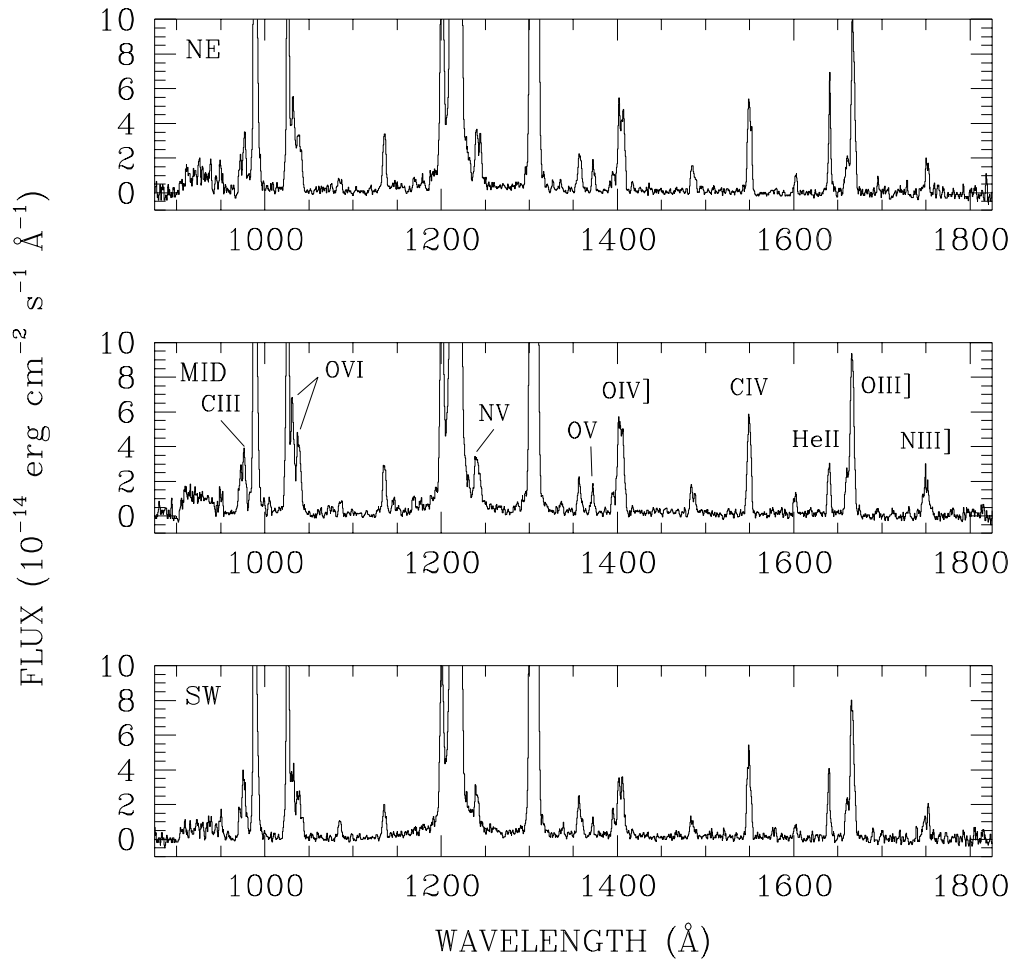


Fig. 3.—

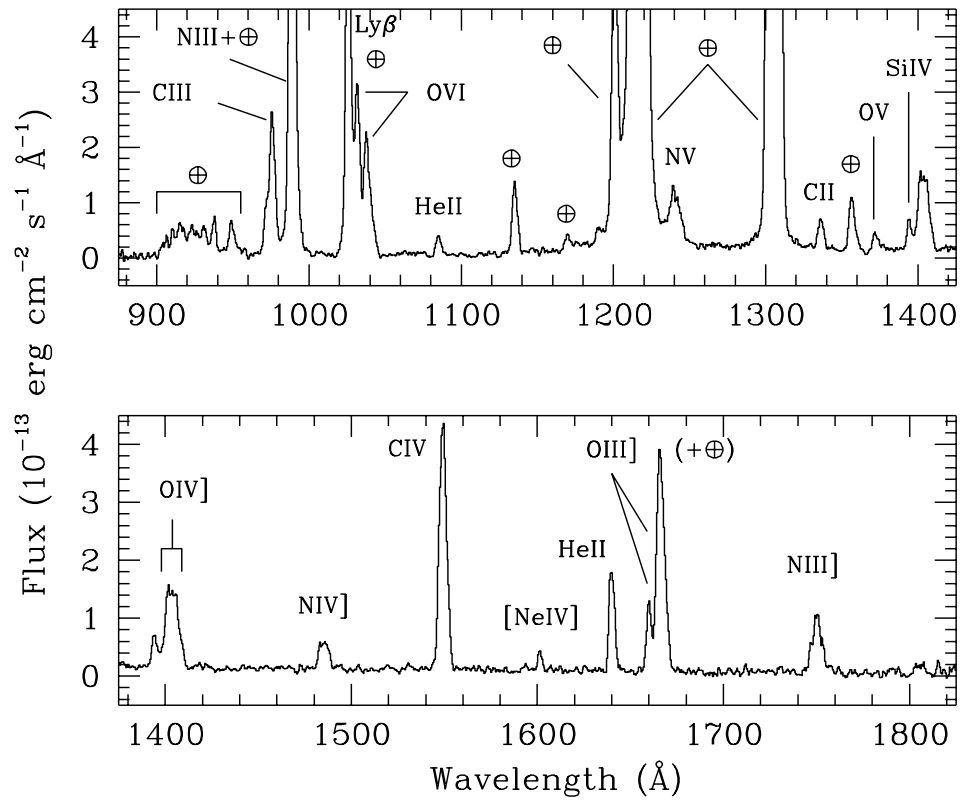


Fig. 4.—

P114:08 FUSE LWRs E1L Overview

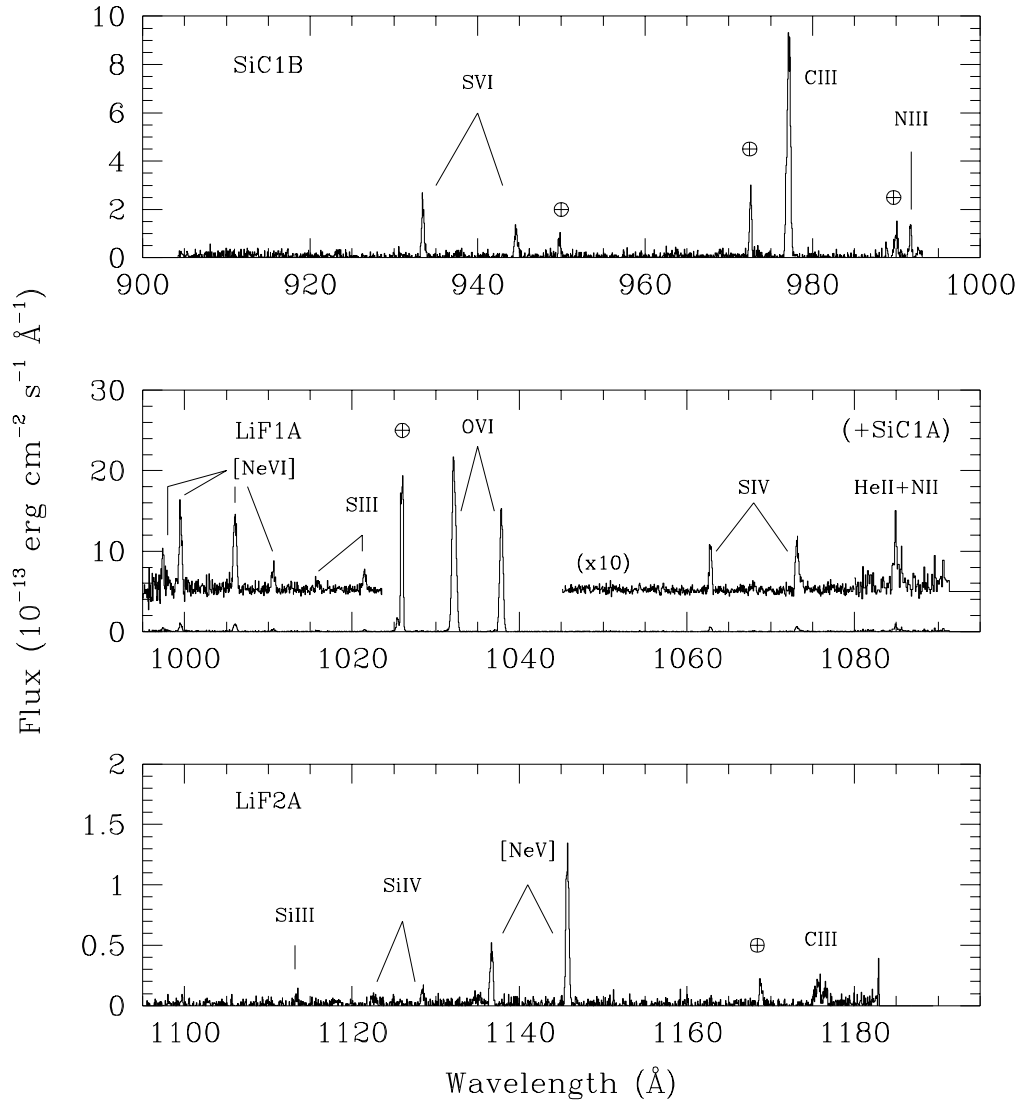


Fig. 5.—

P114:09 FUSE LWRs E2L Overview

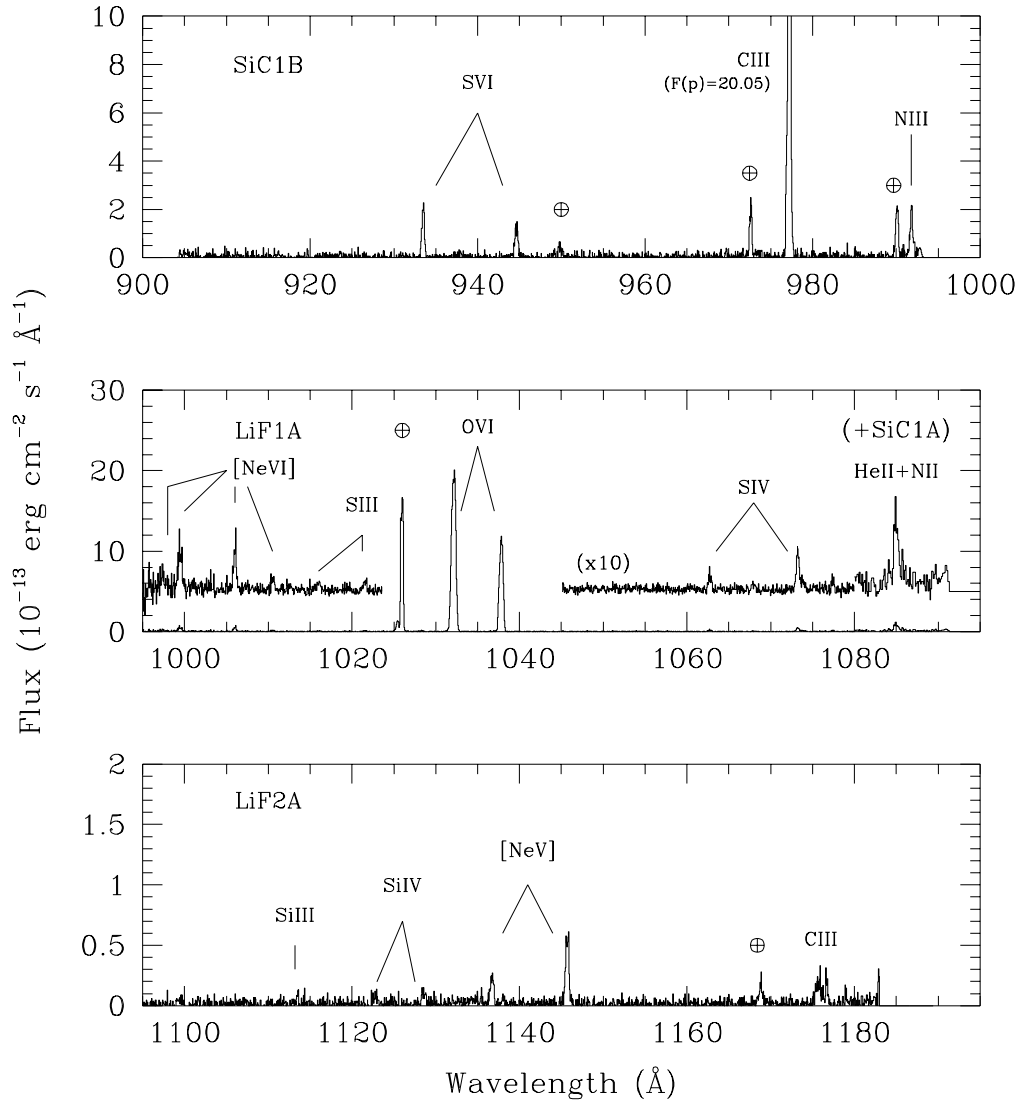


Fig. 6.—

P114:10 FUSE LWRS W1L Overview

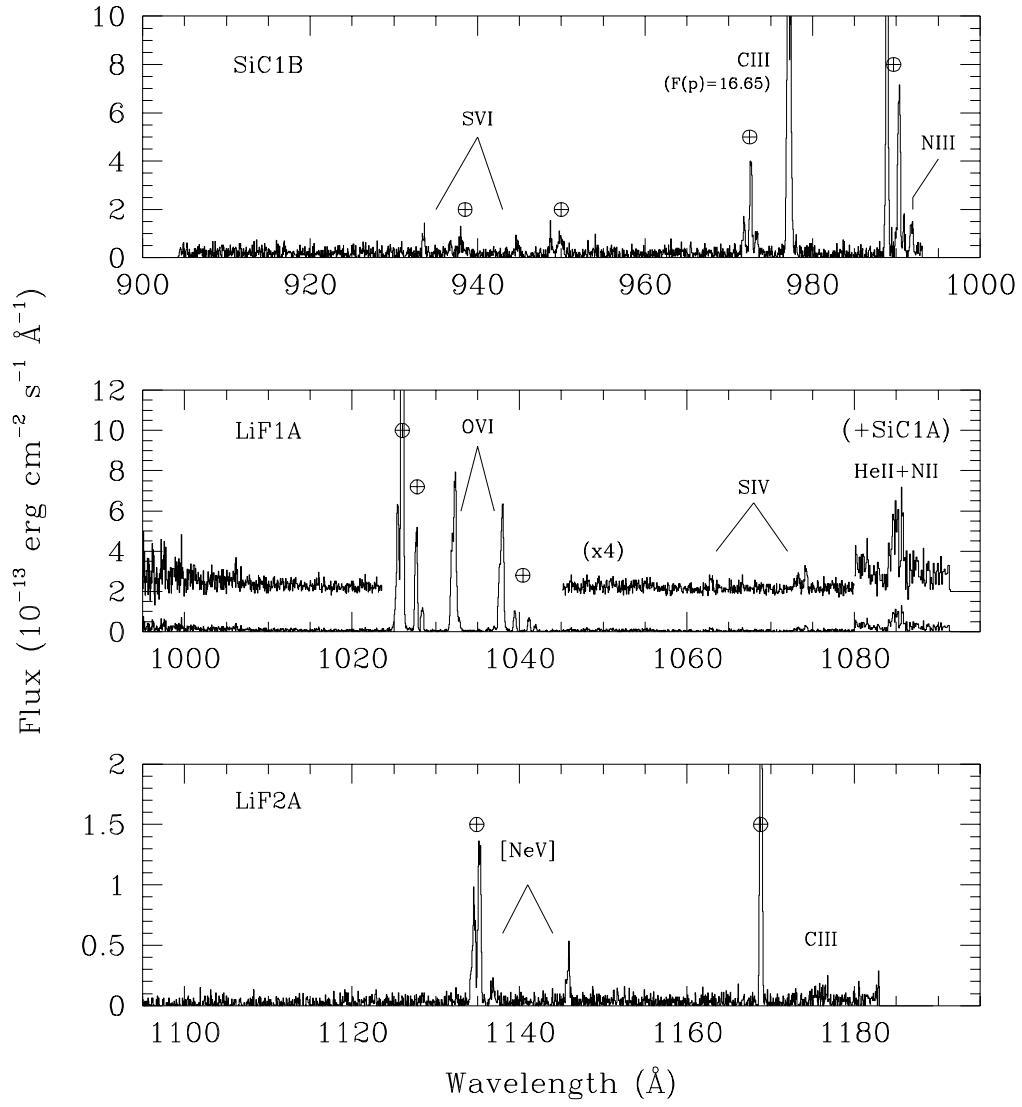


Fig. 7.—

P114:11 FUSE LWRS W2L Overview

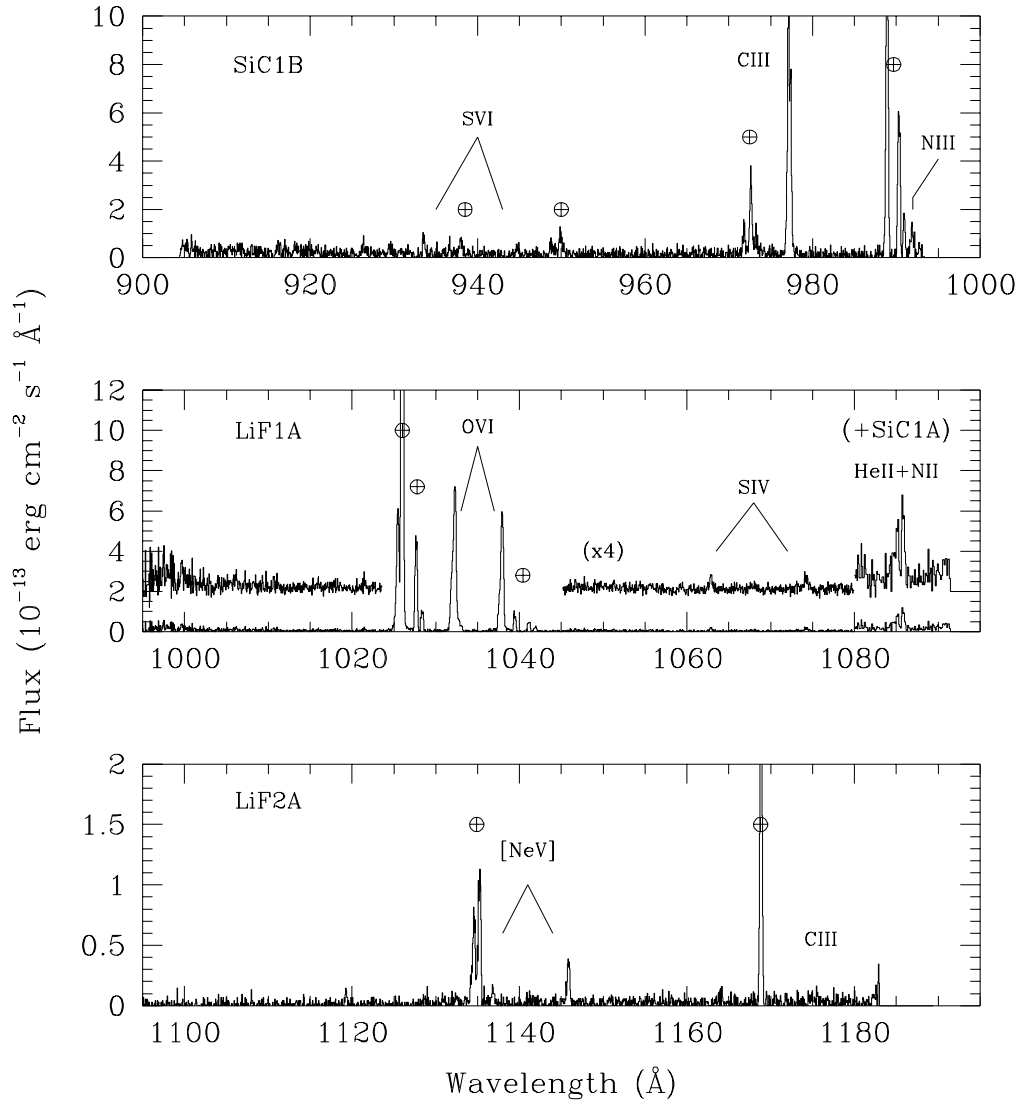


Fig. 8.—

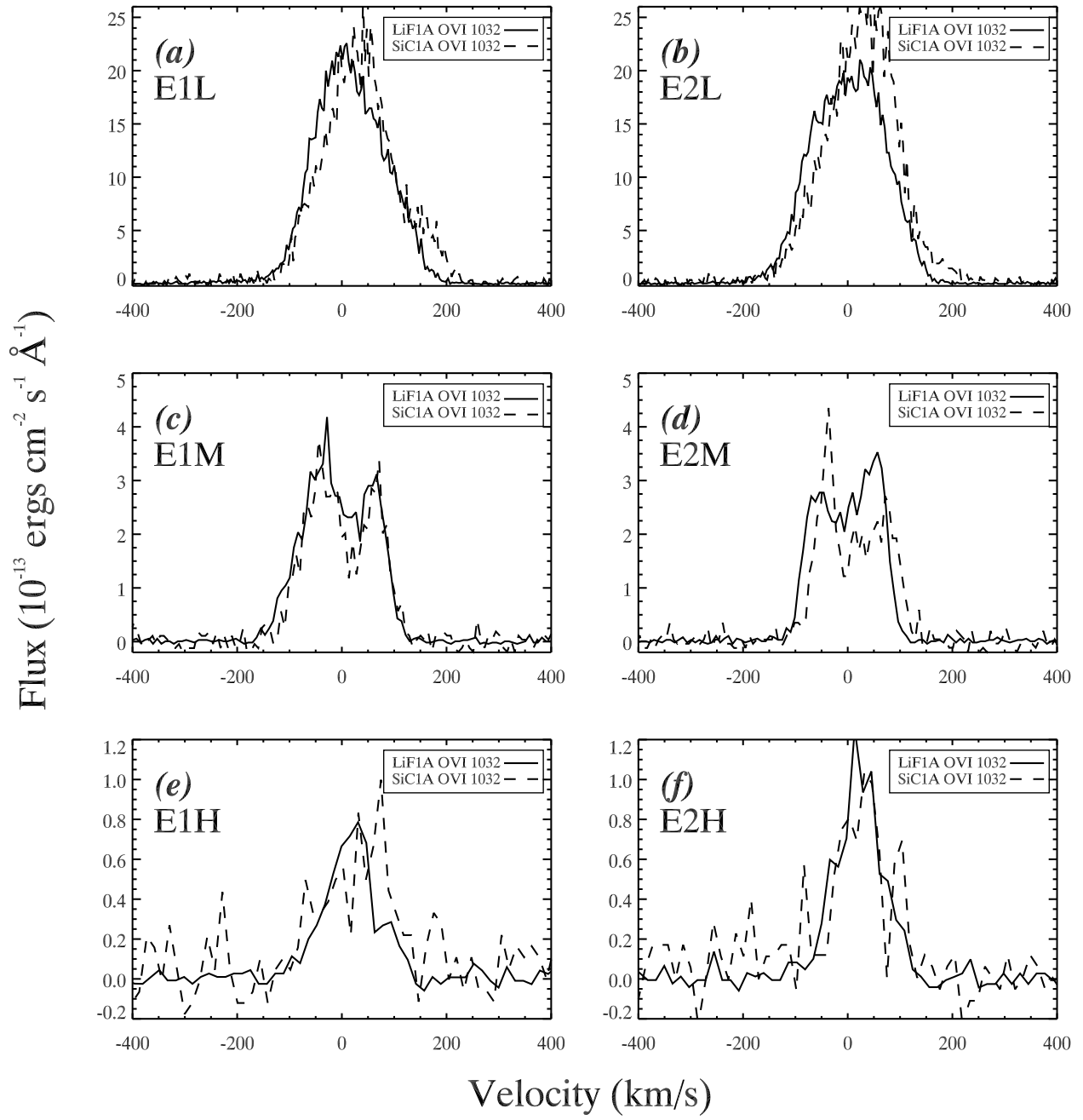


Fig. 9.—

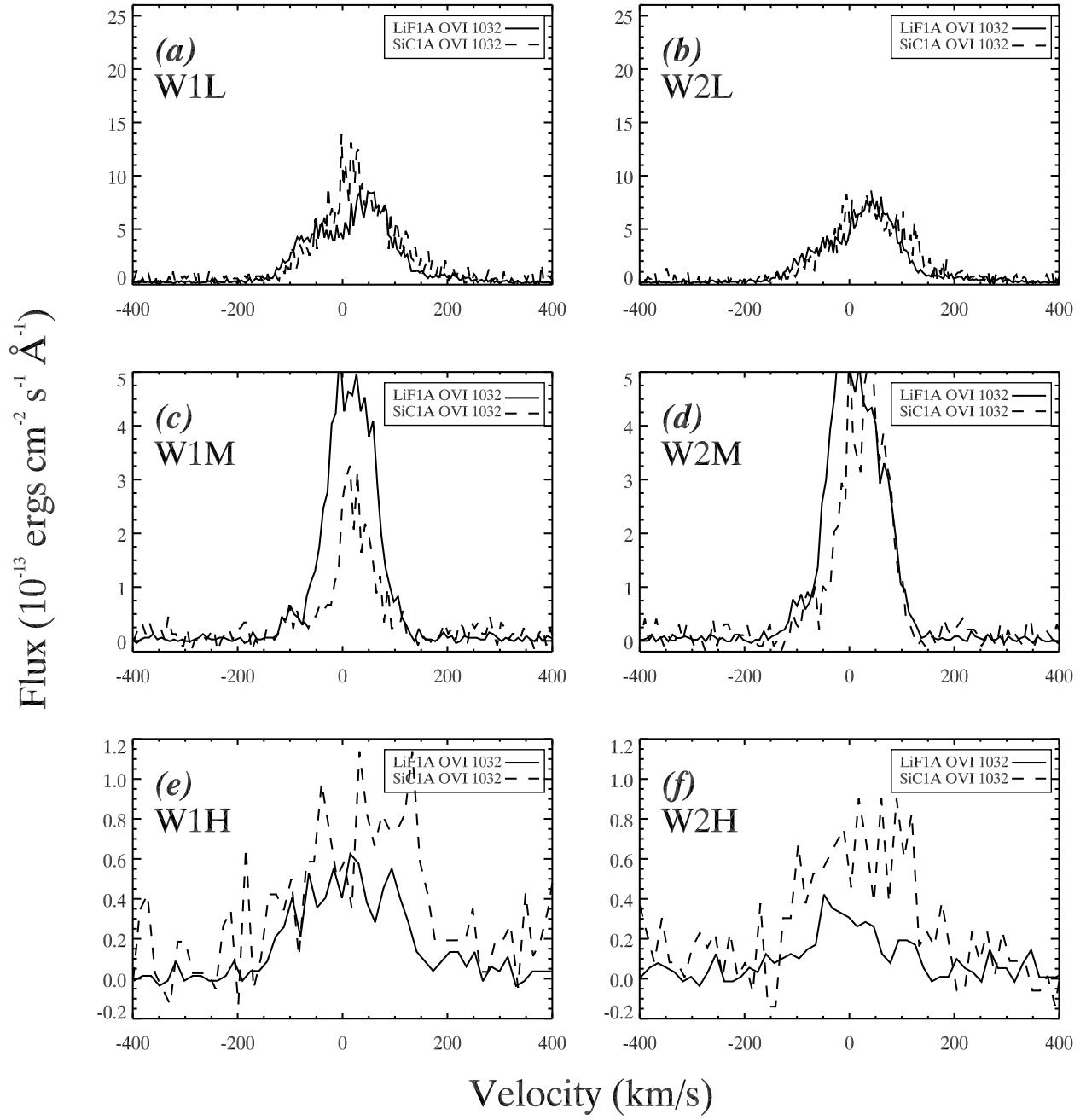


Fig. 10.—

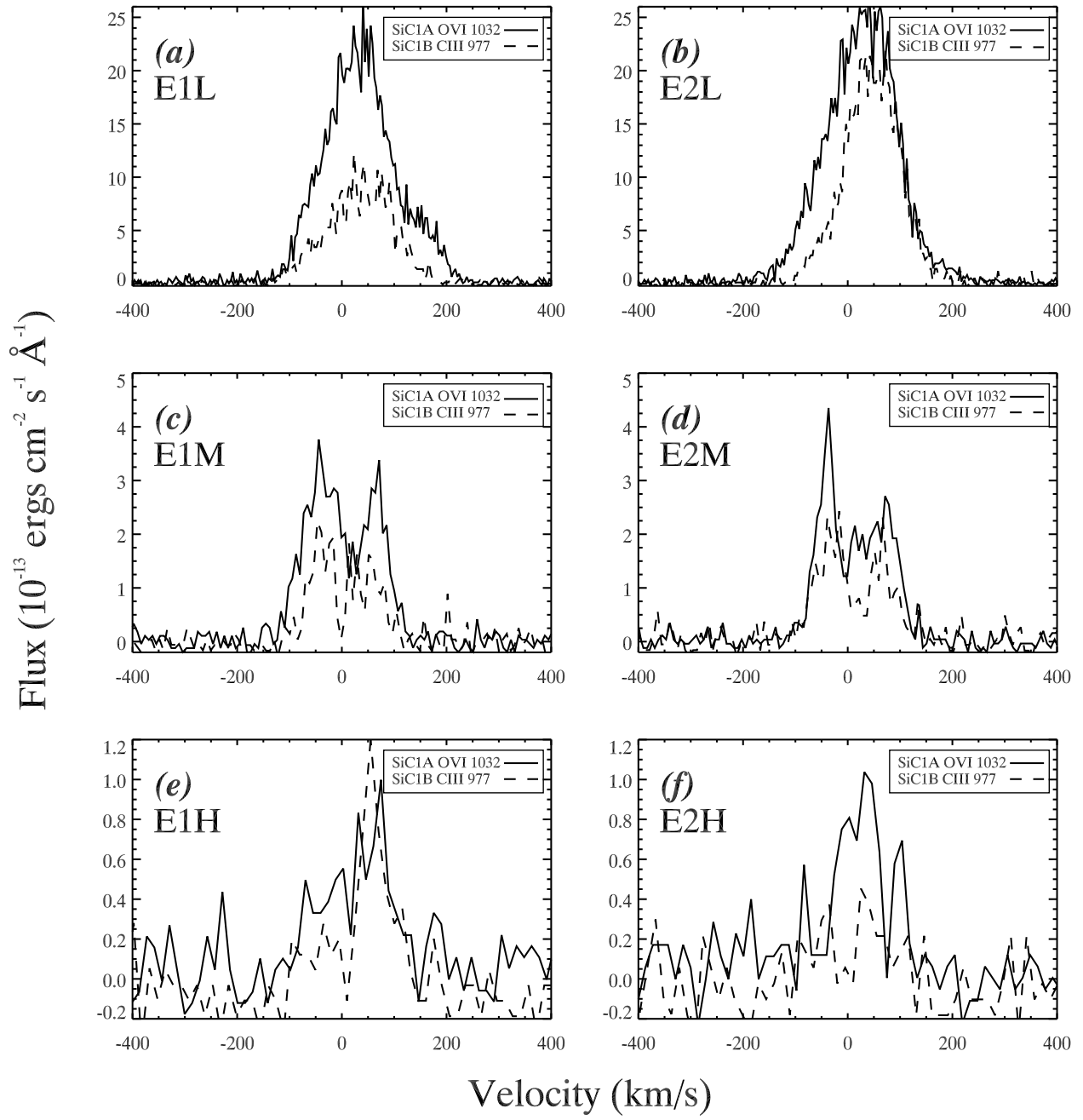


Fig. 11.—

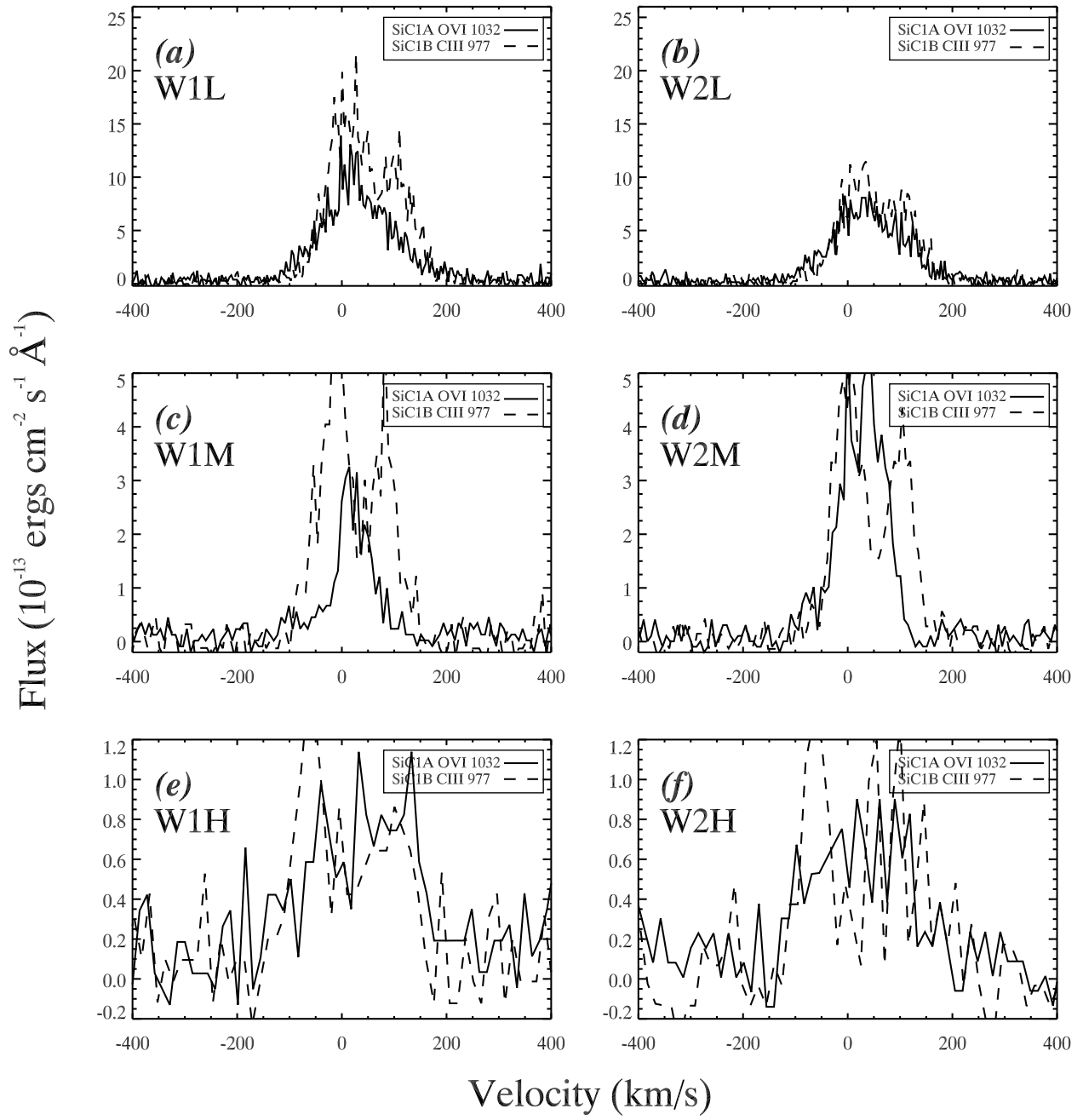


Fig. 12.—

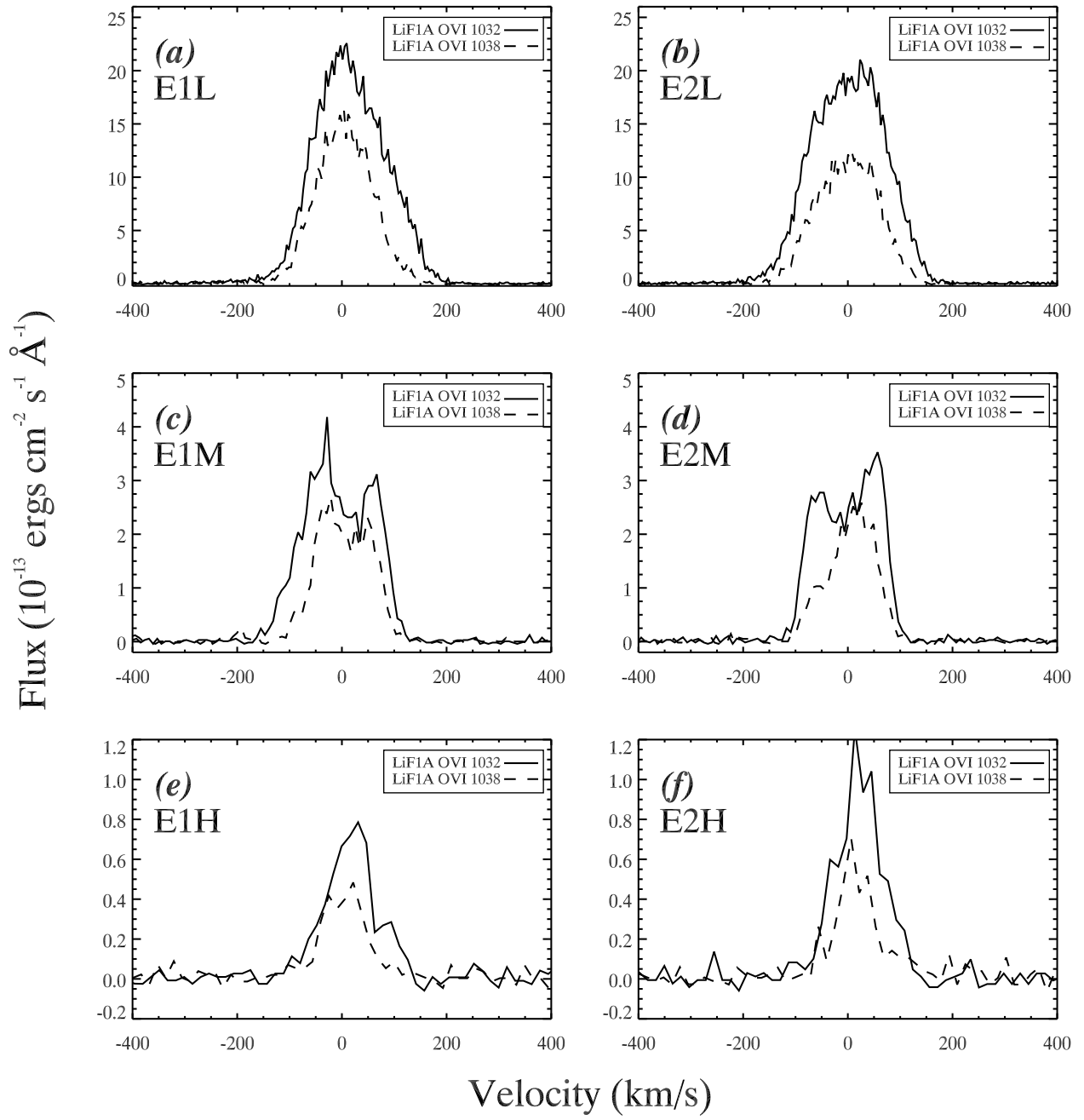


Fig. 13.—

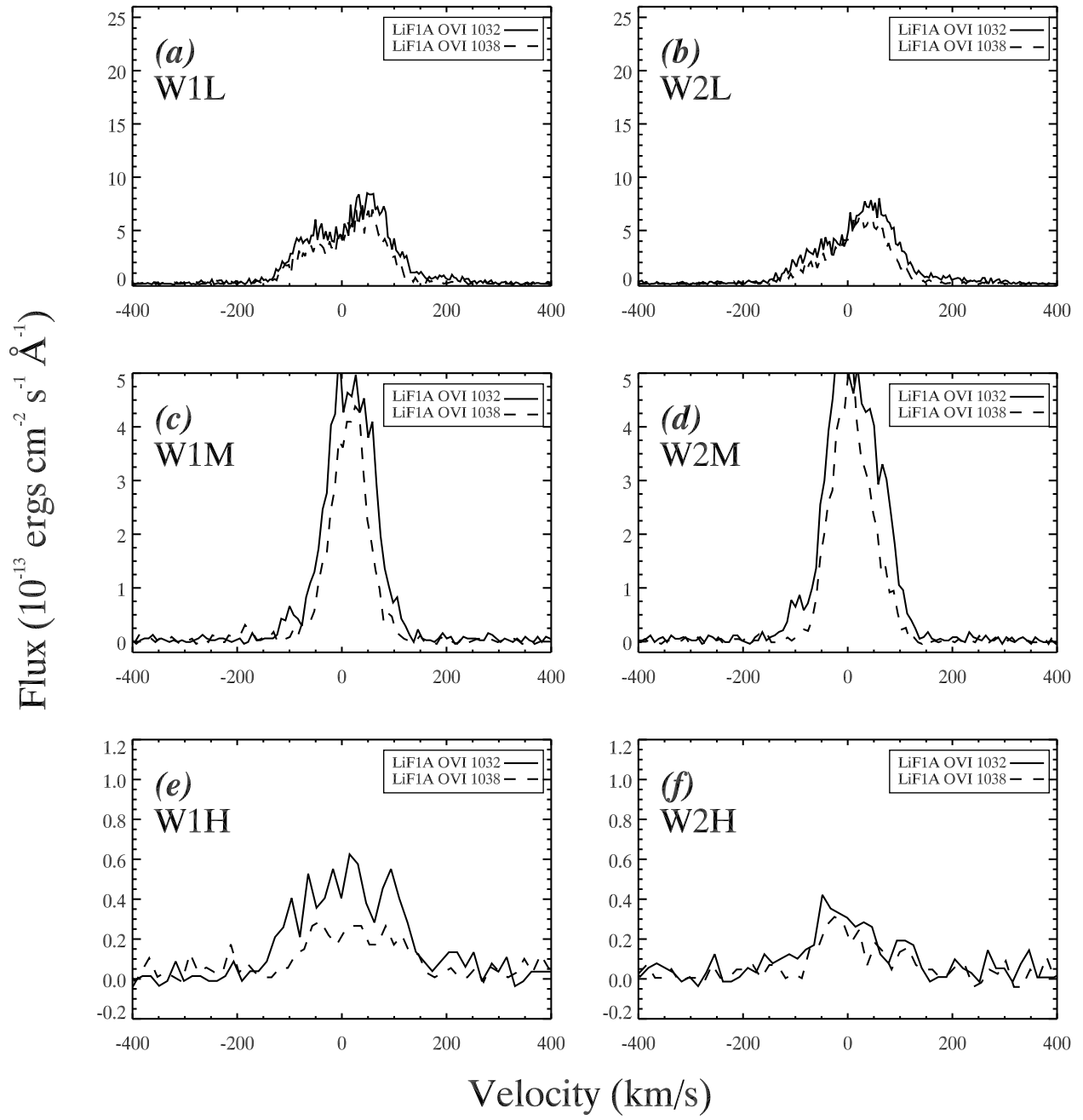


Fig. 14.—

Table 1. Log of Observations

Position ID Obs ID	Coordinates (J2000)	Aperture Position Angle	Date (UT)	Integration Time (s)
HUT-East	20:57:20.9 +31:05:40.1	9" × 116" 45°	1990 Dec. 6	1902 [638] <sup>a</sup>
HUT-E1 (MID)	20:57:20.9 +31:05:40.1	12" circular ...	1995 Mar. 6	1897
HUT-E2 (NE)	20:57:22.9 +31:06:01.7	12" circular ...	1995 Mar. 12	1820
HUT-E3 (SW)	20:57:19.5 +31:05:22.2	12" circular ...	1995 Mar. 16	1755
FUSE-E1M P1140801	20:57:21.3 +31:05:40.1	4" × 20" 214.5°	2000 Sep. 15	12097
FUSE-E1L P1140801	20:57:12.3 +31:02:50.0	30" × 30" 214.5°	2000 Sep. 15	12097
FUSE-E1H P1140801	20:57:17.0 +31:04:19.3	1.25" × 20" 214.5°	2000 Sep. 15	12097
FUSE-E2M P1140901	20:57:22.9 +31:06:01.7	4" × 20" 213.7°	2000 Sep. 16	11747
FUSE-E2L P1140901	20:57:13.8 +31:03:09.1	30" × 30" 213.7°	2000 Sep. 16	11747
FUSE-E2H P1140901	20:57:18.5 +31:04:38.4	1.25" × 20" 213.7°	2000 Sep. 16	11747
HUT-West	20:45:38.4 +31:06:32.6	10" × 56" 0°	1995 Mar. 11	1575
FUSE-W1M P1141001	20:45:38.4 +31:06:32.6	4" × 20" 164.6°	2000 Nov. 8	8538
FUSE-W1L P1141001	20:45:42.7 +31:03:11.9	30" × 30" 164.6°	2000 Nov. 8	8538
FUSE-W1H P1141001	20:45:40.5 +31:04:56.8	1.25" × 20" 164.6°	2000 Nov. 8	8538
FUSE-W2M P1141101	20:45:38.7 +31:06:32.6	4" × 20" 164.4°	2000 Nov. 8	9116
FUSE-W2L P1141101	20:45:43.0 +31:03:11.9	30" × 30" 164.4°	2000 Nov. 8	9116

Table 1—Continued

Position ID Obs ID	Coordinates (J2000)	Aperture Position Angle	Date (UT)	Integration Time (s)
FUSE-W2H P1141101	20:45:40.8 +31:04:56.8	1.25" $\times$ 20" 164.4°	2000 Nov. 8	9116

Note. — Data through three FUSE apertures obtained simultaneously, with the 4"  $\times$  20" MDRS aperture being prime; see text.

<sup>a</sup>Orbital night portion used for analysis.

Table 2. HUT Fluxes for Cygnus Loop Positions<sup>a</sup>

Line ID/ $\lambda$ (Å)	F(East) <sup>b</sup>	F(E1-MID)	F(E2-NE)	F(E3-SW)	F(West)
C III $\lambda$ 977	47.6	86.0	69.3	105	109
O Ia/g + N III $\lambda$ 991 <sup>c</sup>	31.0	417	419	452	...
Ly $\beta$ a/g $\lambda$ 1025 <sup>c</sup>	...	230	180	263	237
O VI $\lambda$ 1032	98.3	85.3	79.7	78.4	128.2
O VI $\lambda$ 1038	52.7	54.7	44.3	46.6	77.8
O VI <sub>tot</sub> $\lambda$ 1035	151	140	124	125	198
He II + [N II] $\lambda$ 1085	5.9	12.2	13.1	24.6	14.5
N V <sub>tot</sub> $\lambda$ 1240	62.6	90.7	79.7	48.0	91.4
C II $\lambda$ 1335	9.9	11.2	5.7	16.3	24.9
O V $\lambda$ 1371	20.2	22.7	22.5	15.9	22.8
Si IV $\lambda$ 1393 <sup>d</sup>	22.4	26.7	15.3	34.7	22.4
O IV] $\lambda$ 1404 <sup>d</sup>	131	159	165	113	98.5
N IV] $\lambda$ 1486	31.0	27.9	30.5	29.8	28.5
C IV $\lambda$ 1549	111	96.7	102	119	182
Ne IV] $\lambda$ 1602	13.5	16.3	15.1	13.1	8.6
He II $\lambda$ 1640	67.0	41.7	66.5	58.0	58.4
O III] $\lambda$ 1661	29.1	29.1	29.1	29.1	29.1
O III] $\lambda$ 1666	70.9	70.9	70.9	70.9	70.9
O III] <sub>tot</sub> $\lambda$ 1664	100	100	100	100	100
O III] <sub>obs</sub> $\lambda$ 1664 <sup>c</sup>	110	187	200	228	194
N III] $\lambda$ 1749	30.6	56.7	27.7	51.6	55.5
F(O III)] $\lambda$ 1664 <sup>e</sup>	17.1 $\pm$ 0.7	3.00 $\pm$ 0.80	2.89 $\pm$ 0.45	2.19 $\pm$ 0.49	11.4 $\pm$ 0.8
Aperture(")	9 $\times$ 116	12	12	12	10 $\times$ 56

<sup>a</sup>Scaling is relative to F(O III)] $\lambda$ 1664 = 100, with conversion to absolute flux and aperture size given at the bottom of the Table.

<sup>b</sup>Astro-1 data from Blair et al. (1991), rescaled to F(O III)] $\lambda$ 1664 = 100.

<sup>c</sup>The strength including contaminating airglow lines are shown for reference.

<sup>d</sup>The O IV and Si IV region has been deblended as described by Blair et al. (1991).

<sup>e</sup>Observed fluxes for O III]<sub>tot</sub>  $\lambda$ 1664 are given in units of  $10^{-13}$  ergs cm<sup>-2</sup> s<sup>-1</sup>.

Table 3. Observed FUSE East LWRS Line Strengths

Ion	$\lambda$	SB(E1L)	SB(E2L)	Channel
S VI	933	8.5	8.7	SiC1B
S VI	944	6.6	6.2	SiC1B
C III	977	54.	99.	SiC1B
	977	52.	85.	SiC2A
N III	991	4.8	8.9	SiC1B
N III	991	4.2	7.6	SiC2A
Ne VI]	997	2.1	1.0	LiF1A
Ne VI]	999	3.8	1.9	LiF1A
Ne VI]	1006	0.4	0.3	LiF1A
Ne VI]	1011	1.4	0.8	LiF1A
S III	1015	5.6	0.5	LiF1A
S III	1021	1.0	0.7	LiF1A
O VI	1032	136.	138.	LiF1A
	1032	130.	140.	LiF2B
	1032	140.	150.	SiC1A
	1032	140.	140.	SiC2B
O VI	1038	78.	70.	LiF1A
	1038	81.	72.	LiF2B
	1038	75.	88.	SiC1A
	1038	79.	83.	SiC2B
S IV	1063	2.3	6.4	LiF1A
S IV	1073	3.4	1.0	LiF1A
He II+N II	1085	5.1	5.4	SiC1A
Si III	1115	0.5	0.4	LiF1B
Si IV	1122	0.8	0.2	LiF1B
Si IV	1127	0.7	0.6	LiF1B
Ne V]	1136	2.0	1.2	LiF1B
Ne V]	1146	5.7	2.8	LiF1B
C III	1176	3.6	3.5	LiF1B

Note. — These are observed values, uncorrected for reddening and absorption. The line strengths are listed as surface brightnesses, in units of  $10^{-17}$  ergs  $\text{cm}^{-2}$   $\text{s}^{-1}$   $\text{arcsec}^{-2}$ .

Table 4. Observed FUSE West LWRS Line Strengths

Ion	$\lambda$	SB(W1L)	SB(W2L)	Channel
S VI	933	4.2	3.0	SiC1B
S VI	944	1.8	1.5	SiC1B
C III	977	87.	54.	SiC1B
	977	71.	46.	SiC2A
N III	991	6.9	5.1	SiC1B
	991	4.2	2.5	SiC2A
Ne VI]	997	2.5	1.1	LiF1A
Ne VI]	999	1.1	0.8	LiF1A
Ne VI]	1006	0.5	0.4	LiF1A
Ne VI]	1011	0.3	0.3	LiF1A
S III	1015	0.3	0.2	LiF1A
S III	1021	...	0.2	LiF1A
O VI	1032	50.	44.	LiF1A
	1032	44.	40.	LiF2B
	1032	58.	47.	SiC1A
	1032	57.	44.	SiC2B
O VI	1038	35.	30.	LiF1A
	1038	34.	30.	LiF2B
	1038	42.	34.	SiC1A
	1038	43.	34.	SiC2B
S IV	1063	0.7	0.5	LiF1A
S IV	1073	0.6	0.2	LiF1A
He II+N II	1085	7.3	8.1	SiC1A
Si III	1115	0.2	0.3	LiF1B
Si IV	1122	...	...	LiF1B
Si IV	1127	...	...	LiF1B
Ne V]	1136	0.7	0.9	LiF1B
Ne V]	1146	1.4	1.2	LiF1B
C III	1176	3.5	5.4	LiF1B

Note. — These are observed values, uncorrected for reddening and absorption. The line strengths are listed as surface brightnesses, in units of  $10^{-17}$  ergs  $\text{cm}^{-2}$   $\text{s}^{-1}$   $\text{arcsec}^{-2}$ .

Table 5. Observed Relative Surface Brightnesses for FUSE Positions<sup>a</sup>

Aperture				
Line ID	E1	E2	W1	W2
MDRS				
O VI $\lambda$ 1032	23.6	20.7	24.4	29.6
O VI $\lambda$ 1038	14.0	11.8	15.9	19.4
C III $\lambda$ 977	9.5	10.9	28.5	25.5
HIRS				
O VI $\lambda$ 1032	11.8	15.6	15.9	8.7
O VI $\lambda$ 1038	6.6	7.9	7.5	6.0
C III $\lambda$ 977	13.5	9.2	26.2	24.1
LWRS				
O VI $\lambda$ 1032	13.6	13.8	5.0	4.4
O VI $\lambda$ 1038	7.8	7.0	3.5	3.0
C III $\lambda$ 977	5.4	9.9	8.7	5.4

Note. — The surface brightnesses are given in units of  $10^{-16}$  ergs  $\text{cm}^{-2}$   $\text{s}^{-1}$   $\text{arcsec}^{-2}$ .

<sup>a</sup>O VI numbers are for the LiF1A channel only. The C III numbers are from the SiC1B channel.